AGU PUBLICATIONS

Tectonics

RESEARCH ARTICLE
10.1002/2016TC004182

Key Points:
- Late Cretaceous-earliest Paleogene hinterland deformation
- Contemporaneous shortening in the foreland side
- Pre-Cenozoic thickened crust in the eastern Tibetan Plateau margin

Supporting Information:
- Supporting Information S1
- Table S1
- Table S2
- Table S3

Correspondence to:
Y. Tian,
y.t.tian@ucl.ac.uk

Citation:
Tian, Y., B. P. Kohn, D. Phillips, S. Hu, A. J. W. Gleadow, and A. Carter (2016), Late Cretaceous–earliest Paleogene deformation in the Longmen Shan fold-and-thrust belt, eastern Tibetan Plateau margin: Pre-Cenozoic thickened crust?, *Tectonics*, *35*, 2293–2312 doi:10.1002/2016TC004182.

Received 7 AUG 2015
Accepted 1 SEP 2016
Accepted article online 10 SEP 2016
Published online 6 OCT 2016

Late Cretaceous–earliest Paleogene deformation in the Longmen Shan fold-and-thrust belt, eastern Tibetan Plateau margin: Pre-Cenozoic thickened crust?

Yuntao Tian[1,2,3], Barry P. Kohn[1], David Phillips[1], Shengbiao Hu[4], Andrew J. W. Gleadow[1], and Andrew Carter[5]

[1]School of Earth Sciences, University of Melbourne, Melbourne, Victoria, Australia, [2]Department of Earth Sciences, University College London, London, UK, [3]Department of Earth Sciences and Geological Engineering, Sun Yat-sen University, Guangzhou, China, [4]State Key Laboratory of Lithospheric Evolution, Institute of Geology and Geophysics, Chinese Academy of Sciences, Beijing, China, [5]Department of Earth and Planetary Sciences, Birkbeck, University of London, London, UK

Abstract This study presents structural and $^{40}Ar/^{39}Ar$ geochronological data from the southern part of the Longmen Shan fold-and-thrust belt that forms the eastern margin of the Tibetan Plateau. Investigations focused on hinterland ductile top-to-the-WNW shear deformation, which has been linked previously to late Cenozoic lower crustal flow. Consistent with previous studies, the sense of deformation is mapped as top-to-the-WNW in the Longmen Shan hinterland. The timing of the deformation is constrained by $^{40}Ar/^{39}Ar$ geochronological data of recrystallized minerals aligned along the shear foliation as Late Cretaceous–earliest Paleogene, thus predating the inferred late Cenozoic crustal flow. This deformation is contemporaneous with SE verging thrusting and loading along the Longmen Shan front, which formed a coeval ~2–3 km thick foredeep sequence along the southwestern margin of the Sichuan Basin. In the context of the regional geology, this tectonic configuration could result from either extrusion of a crustal wedge or back thrust in a duplex. Compared to other orogens, where similar crustal configurations have been reported, it is speculated that the eastern Tibetan Plateau margin acquired thickened crust and highly elevated topography in Late Cretaceous–earliest Paleogene time.

1. Introduction

Numerous studies have sought to explain the formation of the thickened crust and elevated topography of the Tibetan Plateau (see reviews by *Molnar* [1988], *Harrison et al*. [1992], and *Yin and Harrison* [2000]), with a focus on the role of crustal and/or mantle processes following the onset of early Cenozoic Indo-Asia collision [e.g., *England and Houseman*, 1986; *Tapponnier et al*., 2001; *Royden et al*., 2008]. By contrast, a growing number of studies in the central and southern Tibetan Plateau have pointed out that by the end of the Cretaceous, some parts of the central Tibetan Plateau already had thickened crust and elevated topography in response to Mesozoic orogenesis associated with terrane and arc collisions [e.g., *England and Searle*, 1986; *Murphy et al*., 1997; *Kapp et al*., 2003; *Robinson et al*., 2004; *Kapp et al*., 2007].

The eastern Tibetan Plateau margin, which is defined by the NE striking Longmen Shan fold-and-thrust belt, has a thick crust (~60 km) and high topographic relief and has experienced multiple phases of deformation. These include early Mesozoic and late Cenozoic phases of intracontinental orogenesis [*Sichuan Bureau of Geology and Mineral Resources* (*SBGMR)*, 1991; *Burchfiel et al*., 1995; *Chen et al*., 1995; *Tian et al*., 2013; *Wang et al*., 2014] and a period of top-to-the-WNW sense of shear, whose timing is a matter of debate [e.g., *Burchfiel et al*., 1995; *Xu et al*., 2008; *Zhou et al*., 2008]. Despite a long history of deformation, the various models that have been proposed to explain the formation of the thickened crust in the Longmen Shan, such as lower crustal flow [e.g., *Clark et al*., 2005; *Royden et al*., 2008] or crustal shortening and extrusion [e.g., *Hubbard and Shaw*, 2009; *Tian et al*., 2013], have not considered possible contributions from pre-Cenozoic deformation, in part because the timing of these deformation events is poorly constrained.

Given that an explanation for the top-to-the-WNW shear zone has been a key element of previous tectonic models, it is crucial to determine the timing of shearing. Unfortunately, current constraints on the timing are poor. Shearing has been identified on the hinterland side of the Longmen Shan and the Danba Antiform immediately south of the Longmen Shan [*SBGMR*, 1991; *Burchfiel et al*., 1995; *Xu et al*., 2008; *Zhou*

et al., 2008]. Studies of the Danba Antiform interpreted the top-to-the-WNW shearing as resulting from mid Jurassic–early Paleogene (173–160 Ma and 81–47 Ma) postorogenic progressive extension of the Late Triassic orogen [*Zhou et al*., 2008], or Early Cretaceous (~120 Ma) deep crustal extrusion [*Xu et al*., 2008]. Other studies speculated that the shearing in the Longmen Shan hinterland might represent a phase of late Cenozoic extension [*Burchfiel et al*., 1995; *Meng et al*., 2006; *Cook et al*., 2013], driven by outward extrusion of the lower crust [*Burchfiel et al*., 1995, 2008; *Clark et al*., 2005; *Royden et al*., 2008]. To address this question, we conducted a detailed structural and $^{40}Ar/^{39}Ar$ geochronological study on shear structures preserved in the southern Longmen Shan (Figures 1 and 2). The results are interpreted in the context of previous low-temperature thermochronology data in the Longmen Shan, as well as sedimentary and seismic survey data from the foreland Sichuan Basin immediately east of the Longmen Shan.

2. Geological Setting

The regional structural geometry of the Longmen Shan fold-thrust belt is defined by three parallel NW dipping fault zones (Figure 1); from the hinterland (northwest) to the foreland (southeast), these include the Wenchuan-Maowen Fault (WMF), the Yingxiu-Beichuan Fault (YBF), and the Guanxian-Anxian Fault (GAF). Neoproterozoic basement rocks, surrounded by Paleozoic sedimentary strata, outcrop in the core part of the Longmen Shan. To the west of the Longmen Shan lies the Songpan Gaze terrane, which is covered by a thick (>8–10 km) sequence of strongly folded Triassic flysch deposits [*Chang*, 2000; *Roger et al*., 2008; *Ding et al*., 2013]. The Songpan-Ganze terrane was intruded by Late Triassic–Jurassic granitoids and a few Miocene plutons developed along the deep seated Xianshuihe fault, probably in relation to left-lateral slip of the fault (Figure 1) [*Roger et al*., 1995]. Except for Pliocene-Quaternary glacial and fluvial sediments, late Jurassic–Cenozoic strata are absent from this terrane. To the east, the terrestrial Sichuan Basin accommodated >6 km of Late Triassic–Quaternary deposits [*SBGMR*, 1991; *Guo et al*., 1996; *Li et al*., 2003].

In the study area (the southern Longmen Shan), lithological units with different deformation characteristics are separated by several faults (Figure 2a). West of the Longdong fault zone, upper Paleozoic marine limestone-sandstone-mudstone, and Triassic Songpan-Ganze flysch are strongly folded (Figure 2b). The fault zone juxtaposed Ordovician strata over Devonian sequences. Ordovician–Devonian strata within the fault zone are strongly attenuated, forming a tectonic window where the underlying schistose Neoproterozoic rocks crop out (Figure 2a). To the east, in the footwall of the fault zone, Neoproterozoic basement and Paleozoic rocks are strongly mylonitized, schistosed, and faulted. Detailed mapping within this domain suggests a phase of top-to-the-WNW shearing (see section 3 for details). Farther east, Neoproterozoic basement rocks exposed between the Wulong and Xiaoguanzi faults, which are southern extensions of the WMF and YBF, respectively [*Burchfiel et al*., 1995; *Tao*, 1999], are less deformed, or undeformed (Figure 2). Note that the Xiaoguanzi fault is also locally named as the Erwangmiao fault [e.g., *Cook et al*., 2013]. East of the Xiaoguanzi fault, terrestrial Triassic to Quaternary sediments are folded and faulted. In following sections, local fault nomenclature (Wulong and Xiaoguanzi faults) in the southern LMS will be replaced by the YBF and WMF, which have been more widely used in previous literature.

The Longmen Shan fold-thrust belt experienced two phases of orogenic shortening in the early Mesozoic and later Cenozoic, respectively [e.g., *Burchfiel et al*., 1995; *Yan et al*., 2011]. The first shortening phase is SE-SSE verging, as expressed by structures at different scales. Kilometer-scale klippe structures developed in both the Longmen Shan front and hinterland (Figure 2a). Along the Longmen Shan front, Neoproterozoic basement and Paleozoic rocks tectonically overlie Late Triassic–Cretaceous sedimentary rocks; and on the western, hinterland side of the Longmen Shan strongly folded Triassic flysch sediments tectonically overlie Permian rocks. These allochthonous blocks were formed by SSE verging thrusting of the Longmen Shan fold-thrust belt and the Songpan-Ganze terrane. At a meter scale, tight folds (F1) in the Triassic flysch and Paleozoic rocks indicate NNW-SSE shortening of the Longmen Shan hinterland (Figure 2b). Within the early Paleozoic and Precambrian rocks on the hinterland side, structures such as boudinaged sandstone and/or quartz vein and S-C fabrics indicate SE directed thrusting.

The timing of the first phase of shortening is well constrained. First, the presence of klippen of Paleozoic and Precambrian rocks over Triassic sediments in the Longmen Shan front indicates that these structures were formed during the Late Triassic or later (Figures 2a and 2d). Second, geochronological data suggest that deformation had initiated before or at 237–190 Ma [*Huang et al*., 2003; *Weller et al*., 2013]: (i) the oldest U–Th–Pb

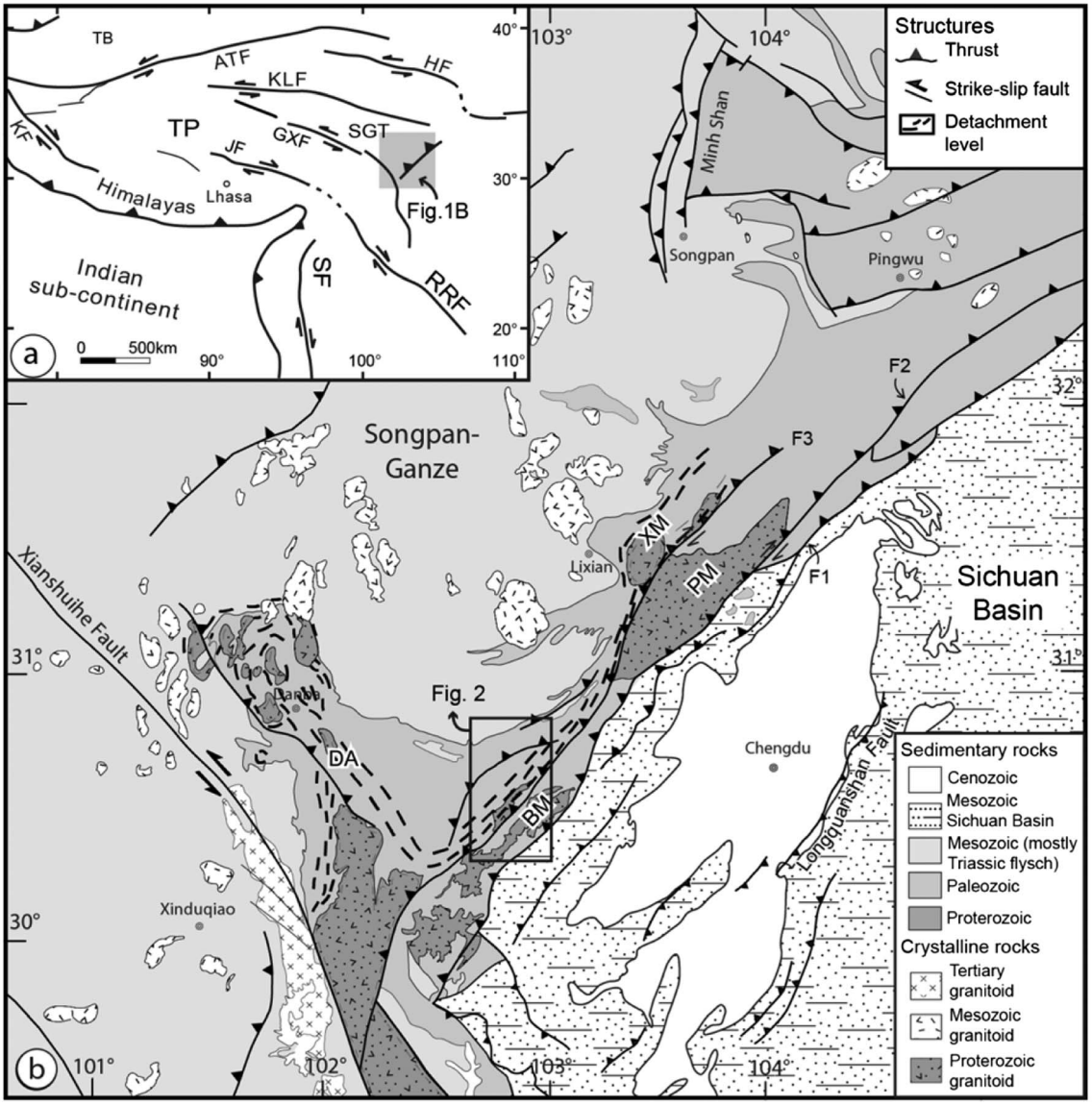

Figure 1. (a) Tectonic map showing the main structures of the Tibetan Plateau and location of the study area (shaded square). Abbreviations: ATF = Altyn Tagh Fault, DA = Danba Antiform, GXF = Ganzi-Xianshuihe Fault, HF = Haiyuan Fault, JF = Jiali Fault, KLF = Kunlun Fault, KF = Karakorum Fault, RRF = Red River Fault, SF = Sagaing fault, SGT = Songpan-Ganze terrane, TB = Tarim Basin, and TP = Tibetan Plateau. (b) Generalized geological map of the Longmen Shan, modified after *SBGMR* [1991], *Burchfiel et al.* [1995], and *Tian et al.* [2013]. Also shown is the location of Figure 2. F1 = Guanxian-Anxian Fault, F2 = Yingxiu-Beichuan Fault, F3 = Wenchuan-Maowen Fault, BM = Baoxing massif, PM = Pengguan massif, and XM = Xuelongbao massif.

monazite and Sm–Nd garnet ages (204–190 Ma), derived from metamorphosed rocks in the Danba Antiform, immediately south of the Longmen Shan, were interpreted as dating the timing of Barrovian metamorphism associated with the deformation [*Huang et al.*, 2003; *Weller et al.*, 2013] and (ii) $^{40}Ar/^{39}Ar$ dating of early Paleozoic schistose rocks from the northern Longmen Shan yielded ages between 237 and 208 Ma, which were interpreted as minimum age constraints for Mesozoic shortening [*Yan et al.*, 2011]. Third, Late Triassic flexural subsidence of the western Sichuan Basin, which accommodated >4 km thick sediments in the foredeep, achieved the eastward loading and shortening along the Longmen Shan.

In late Cenozoic time, the Longmen Shan fold-thrust belt was reactivated [e.g., *Burchfiel et al.*, 1995; *Wang et al.*, 2012; *Tian et al.*, 2013]. This latest shortening is brittle and SE-SSE verging, forming numbers of brittle faults, slickenlines, and widely developed fractures in the basement and Paleozoic rocks in the Longmen Shan. In the Longmen Shan front and southwestern Sichuan Basin, Eocene, Oligocene, and Quaternary strata were folded and faulted [e.g., *SBGMR*, 1991; *Burchfiel et al.*, 1995; *Jia et al.*, 2006]. These structures and the

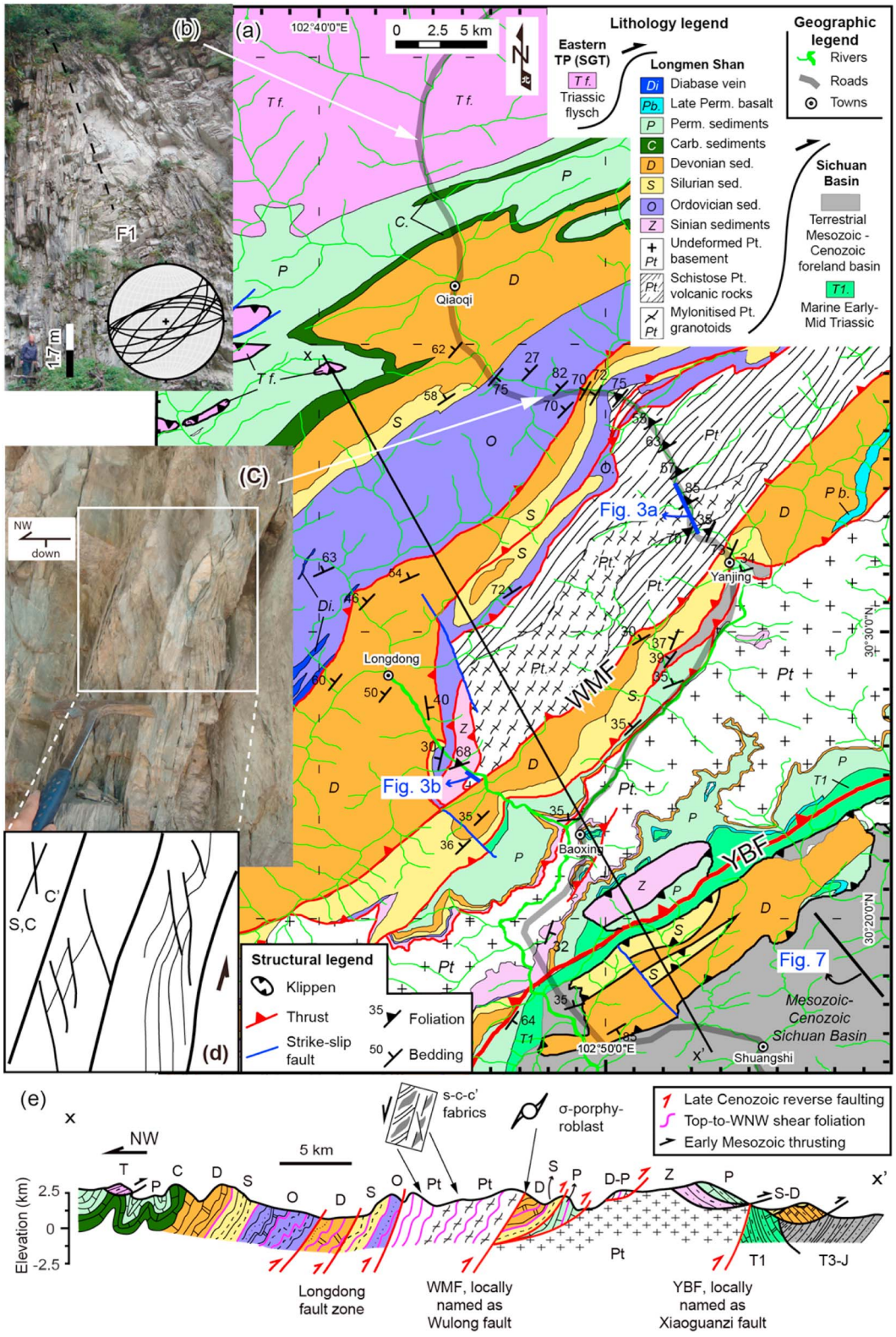

Figure 2. (a) Detailed geological map of the southern Longmen Shan that combines our mapping results with the geological map of the Baoxing area (scale: 1:200,000) [*SBGMR*, 1976]. Labels for lithological units are explained in the legend. (b) View to the west of an overturned fold (F1) in Triassic flysch with stereographic projection of the F1 fold axial planes representative of the folding in Triassic flysch in the southern Longmen Shan hinterland. This indicates that D1 deformation results from NNW-SSE shortening. (c) Southwestward view of early Paleozoic sandstone that outcrops west of the WMF fault zone. (d) S-C-C′ fabrics showing a top-to-the-NW sense of shear. (e) Geological section (X-X′ in Figure 2a) across the southern Longmen Shan.

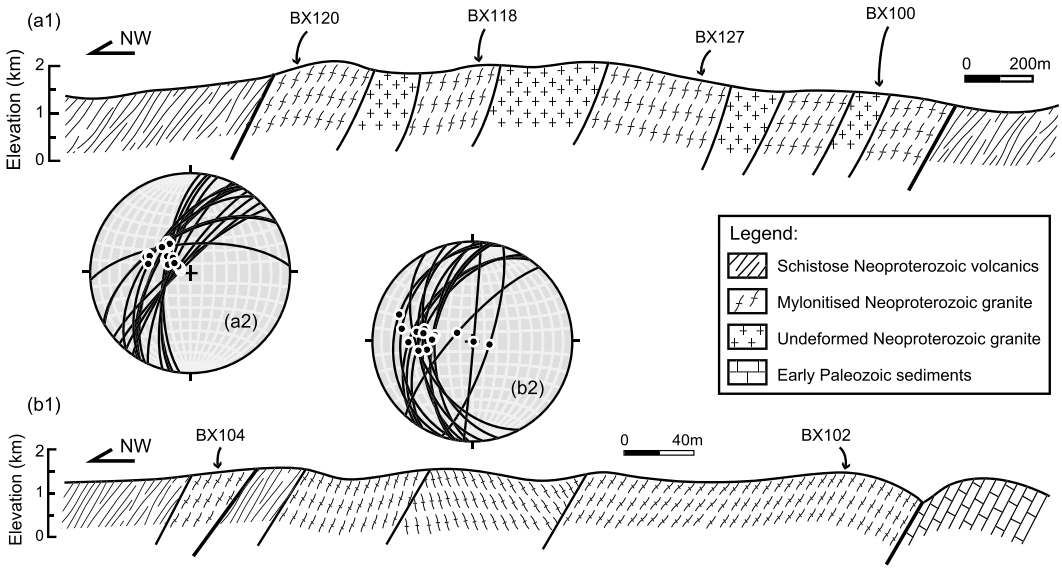

Figure 3. Two cross sections (a1 and b1), showing detailed geology of the mylonite belt with locations of samples collected for $^{40}Ar/^{39}Ar$ geochronology. Also shown are the (a2 and b2) stereographic projections of the top-to-the-WNW shear foliation and lineation measured at sites along the (a1 and b1) cross sections, respectively. The locations of these cross sections are shown in Figure 2. For clearer illustration of the profiles, the horizontal axes of panel a1 and b1 have been exaggerated by ~8 and ~40 times, respectively.

evidence for active faulting [e.g., *Densmore et al*., 2007; *Zhang et al*., 2010] have been interpreted as a response to Cenozoic intracontinental shortening [e.g., *Tian et al*., 2013]. Further, several low-temperature thermochronology studies suggest that the Longmen Shan experienced a phase of enhanced exhumation in the late Cenozoic [*Kirby et al*., 2002; *Godard et al*., 2009; *Wang et al*., 2012; *Cook et al*., 2013; *Guenthner et al*., 2014] and that the pattern of exhumation is controlled by the main faults [*Tian et al*., 2013]. Worth noting is that Late Cenozoic sediments are absent along the Longmen Shan front. This may indicate that the shortening is not significant [*Burchfiel et al*., 1995]. It is also possible that the sediments were once deposited and later removed by regional denudation in the Sichuan Basin, which experienced ~1–5 km unroofing since Oligocene time, as indicated by thermal history modeling of low-temperature thermochronological data [*Richardson et al*., 2008; *Tian et al*., 2012a, 2012b].

3. Top-to-the-Hinterland Shear and Coeval top-to-the-Foreland Shortening

Except for early Mesozoic and late Cenozoic phases of foreland-verging shortening, summarized above, a further set of deformation features characterized by top-to-the-hinterland shear has been briefly reported in the southern Longmen Shan by previous studies [*Burchfiel et al*., 1995; *Xu et al*., 2008]. We expand on this observation through detailed structural mapping along two fluvial valleys (Figure 2a), presented below.

3.1. Top-to-the-Hinterland Shear

A belt of top-to-the-WNW shear deformation is mapped within Precambrian and Paleozoic rocks exposed east of the Paleozoic cover sediments (Figures 1–3), as shown by various features at different scales in different rocks. On a regional scale, the deformation may have extended more than 200 km from the southern Longmen Shan to the Danba Antiform, forming a continuous ductile top-to-the-WNW detachment fault (Figure 1). At a local scale, top-to-the-WNW shear foliations, mineral stretching lineations, quartz boudinage features, and a variety of deformation fabrics (e.g., S-C-C′ fabrics, asymmetric folds) are observed in mylonized and/or schistose Neoproterozoic basement and early Paleozoic rocks east of the Longdong fault zone (Figure 4).

The strongest deformation related to the shear was developed in the mylonitized and schistose Neoproterozoic basement rocks exposed immediately west of the WMF (Figures 2–4). Within these rocks, mylonites with different matrix-to-porphyroblast ratios were developed (Figures 4a and 4d). Aspect ratios of elongated minerals range between 2 and 10. Kinematic indicators (e.g., asymmetric fold, S-C-C′ fabrics,

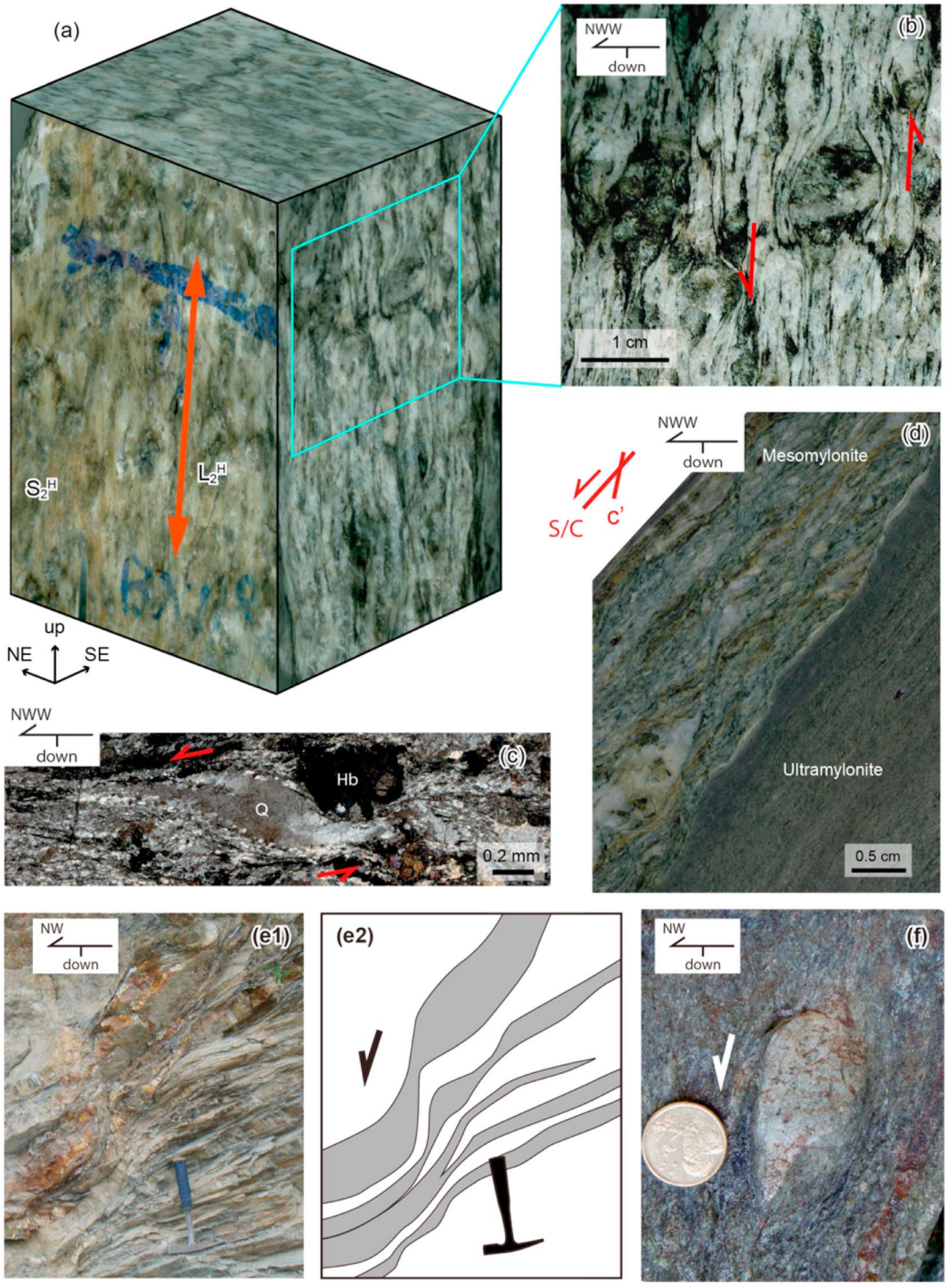

Figure 4. Characteristic kinematic indicators for top-to-the-WNW shearing. (a) Block view showing top-to-the-WNW shear foliation and stretching lineation on the foliation surface (sample BX118) and kinematic indicators on the facet parallel to the lineation and normal to the foliation. (b) Close-up view of the left-lateral sigmoidal granitic porphyroblast shown in Figure 4a. (c) Sigmoidal quartz porphyroblast showing top-to-the-WNW-ward sense of shear (sample BX118). (d) Polished surface showing contact between mylonite with different matrix-to-porphyroclast ratios. S(C)-C′ fabric in the relatively coarser mylonite shows top-to-the-WNW sense of shear (sample BX104). Southwestward view of boudinaged sandstone interbedded with mudstone (outcropping immediately east of the WMF fault zone), showing top-to-the-NW-ward shear (e1 and e2). Panel e2 is schematic of e1. (f) left-lateral sigmoidal feldspar porphyroblast in mylonitized Neoproterozoic volcanic rock. See Figure 3 and Table 1 for sample locations.

Table 1. Locality, Petrographic, and Microstructural Data of Dated Samples[a]

Sample No.	Lithology	Location (°E/°N)	Mineral Assemblage	Dated Minerals	Grain Size (μm)	Microdeformation Features in Quartz (Q) and Feldspar (Fds)
BX100	Undeformed granite	102.886/30.559	Q + Fds + Bt + Wm + Chl	Bt	>300	-
BX102	Granitic mylonite	102.762/30.414	Q + Fds + Agg + Hb + Chl	Agg	<5	Tapering deformation twins and kink bend for fds; Undulose extinction and recrystallized subgrain for Q
BX118	Granitic mylonite	102.880/30.574	Q + Fds + Bt + Wm + Chl	Bt, Wm	180–250	Brittle fracture for Fds; Undulose extinction and recrystallized subgrain for Q
BX120	Biotite schist	102.878/30.579	Bt + Q + Wm + Chl	Bt	180–250	Undulose extinction and recrystallized subgrain for Q
BX127	Granitic mylonite	102.883/30.566	Q + Fds + Bt + Wm + Chl	Bt, Wm	180–250	Brittle fracture for Fds; Undulose extinction and recrystallized subgrain for Q

[a]Mineral abbreviations: Agg = aggregate, a mixture of fine-grained white mica, quartz, and feldspar; Bt = Biotite; Chl = Chlorite; Fds = Feldspar; Hb = Hornblende; Wm = white mica; and Q = Quartz.

and sigmoidal objects) suggest a top-to-the-WNW sense of deformation (Figures 4a and 4b). These observations, on an outcrop scale, are consistent with those microstructures at both millimeter (Figure 4c) and micrometer scales (lattice preferred orientation of quartz) [*Xu et al*., 2008]. Furthermore, within the mylonite zone, undeformed Neoproterozoic basement rocks are also observed (Figures 3a1).

West of the mylonite zone, in the interbedded limestone-sandstone-mudstone Paleozoic cover rocks, the top-to-the-WNW shear foliation is parallel with the bedding (Figure 2). In these layers brittle-ductile deformation features, such as boudinaged sandstone layers and S-C-C′ fabrics, showing top-to-the-WNW directed shear, were developed (Figure 2c). Early Paleozoic strata immediately west of the mylonitized pre-Cambrian rocks are considerably thinner than those exposed in areas to the south and north (Figures 2a and 2e). This attenuation zone has been named as the Longdong fault [e.g., *Tao*, 1999].

Within the Paleozoic cover rocks, exposed immediately east of the WMF, boudinaged sandstone layers showing top-to-the-NW shear features are also observed (Figures 4e1 and 4e2). These deformed Paleozoic rocks are thought to be allochthonous in nature and were juxtaposed above the eastern sheet of the basement rocks during late Cenozoic SE verging thrusting (see section 5.2 for details).

The shear foliation and mineral stretching lineations dip and plunge mostly W-NW (Figures 3 and 4a), but occasionally toward the E-SE, and probably formed by tilting of the original foliation during late Cenozoic faulting (Figure 3).

Mylonitization associated with shearing occurred under greenschist-facies conditions. The mineral assemblages defining the foliation and/or lineation fabrics within the mylonitized basement rocks include quartz + feldspar + biotite + white mica + chlorite (Table 1), i.e., no high-grade metamorphic minerals were observed. Further, brittle-ductile deformation is common in most minerals (Figure 5). For example, feldspar deformation is dominantly brittle, forming structures such as tapering deformation twins, kink bends, and grain breakage (Figures 5a and 5c). However, quartz in the mylonite was deformed ductily, as indicated by sigmoidal structures, undulose extinction in remnant quartz, and recrystallized quartz produced by subgrain rotation (SGR) (Figures 5b–5e).

Previous temperature calibrations on quartz and feldspar deformation suggest that recrystallized quartz is formed by subgrain rotation (SGR) under low–medium-grade conditions with deformation temperatures between 400 and 500°C whereas undulose extinction in remnant quartz forms at lower temperatures (<300–400°C) [e.g., *Stipp et al*., 2002; *Passchier and Trouw*, 2005]. Tapering deformation twins and kink bends in feldspar occur at similar deformation temperatures (400–500°C) [e.g., *Ji et al*., 1998; *Passchier and Trouw*, 2005]. Therefore, the mineral assemblages and microdeformation features described above suggest that deformation temperatures of the top-to-the-WNW shear may have reached a maximum temperature of 400–500°C and most likely occurred at 300–450°C. This suggests that shear deformation occurred at a crustal depth of ~15–20 km, assuming a typical geothermal gradient of 20–30°C/km for an orogenic belt [*Pollack et al*., 1993; *Hu et al*., 2000; *Xu et al*., 2011].

The timing of top-to-the-WNW shear is Late Cretaceous–early Paleogene, as constrained by new $^{40}Ar/^{39}Ar$ data presented in section 4 below.

3.2. Coeval top-to-the-Foreland Shortening

On the foreland side, a phase of SE directed Late Cretaceous–early Paleogene shortening can be inferred from previously reported seismic profiles and the depositional history of the southwestern Sichuan Basin [*Guo et al*., 1996; *Jia et al*., 2006]. In the southwestern Sichuan Basin and areas farther south, a belt of Late Cretaceous–early Paleogene depocenters, running parallel to the Longmen Shan strike, developed (Figure 6). The coeval paleocurrent direction was eastward, indicating that the Longmen Shan and Songpan-Ganze terrane were the main sediment sources. The Late Cretaceous–early Paleogene basins are interpreted as foreland basins, formed by crustal overloading along frontal thrusts of the Longmen Shan fold-thrust belt [*SBGMR*, 1991; *Guo et al*., 1996].

Evidence for this phase of shortening along the Longmen Shan front is strongly supported by coeval growth strata revealed by seismic studies [*Jia et al*., 2006] (Figure 7). The Late Cretaceous–early Paleogene age of sediments in the southwestern Sichuan Basin is well constrained by both paleomagnetic [*Zhuang et al*., 1988; *Enkin et al*., 1991; *Huang and Opdyke*, 1992] and paleontological data [*SBGMR*, 1991; *Guo et al*., 1996]. This evidence suggests that the Late Cretaceous–early Paleogene shortening is contemporaneous with the top-to-the-WNW shear the Longmen Shan hinterland side.

4. Sampling and Analytical Strategies

$^{40}Ar/^{39}Ar$ geochronology has been used to constrain the timing of the deformation. The dated samples cover the two main kinds of deformed rocks in the shear zone, namely, mylonite and schist. One undeformed granite sample from the zone was also dated for comparison. All samples were collected from two transects in the southern and northern portions of the shear zone (Figures 2 and 3), where outcrops are fresh and deformation indicators are clear. Detailed location information and petrographic features for the samples are listed in Table 1.

Biotite and white mica in the sheared samples are elongated and aligned along the foliation. Their dimensions are about 100–300 μm wide by > 300 μm long (Figures 5c–5e). No inherited euhedral grains were observed. Biotite in the undeformed sample (BX100) is subhedral and coarse grained, ~400 μm in both width and length. Biotite in both deformed and undeformed samples is brown to green in color and has been partly chloritized.

White mica and biotite separates as well as a fine-grained mineral aggregate (sample BX102 only) were prepared for $^{40}Ar/^{39}Ar$ geochronology using standard crushing, sieving, electromagnetic, and heavy liquid mineral separation techniques. Each separate was then handpicked to the highest level of purity possible. Electron microprobe analyses (EMPA) were carried out on representative grains to quantify the composition of minerals used for $^{40}Ar/^{39}Ar$ analysis. Analyses were made on both grain margin and interior, and because no chemical zoning was observed, data from different grain areas are not distinguished.

Analytical methods for EMPA and $^{40}Ar/^{39}Ar$ analyses are detailed in Texts S1 and S2 in the supporting information, respectively, and the resulting data are listed in the supporting information Tables S1, S2 and S3, respectively.

5. Results and Interpretation

5.1. EMPA Results

The K_2O versus SiO_2 plot differentiates the mineral aggregate, white mica, and biotite samples (Figure 8 and Table S1). The mineral aggregate of sample BX102 shows significant variation in SiO_2 and K_2O, ranging from 25 to 98 wt % and from 0 to 11 wt %, respectively (Figure 8a). These results are consistent with petrographic observations that the aggregate consists of a mixture of mica, feldspar, and quartz. White mica in samples BX118 and BX127 has SiO_2 and K_2O content of 46–58 wt % and 10–12 wt %, respectively, whereas biotite shows relatively lower SiO_2 and K_2O content of 32–42 wt % and 7–10.3 wt %, respectively (Figure 8b and Table S1).

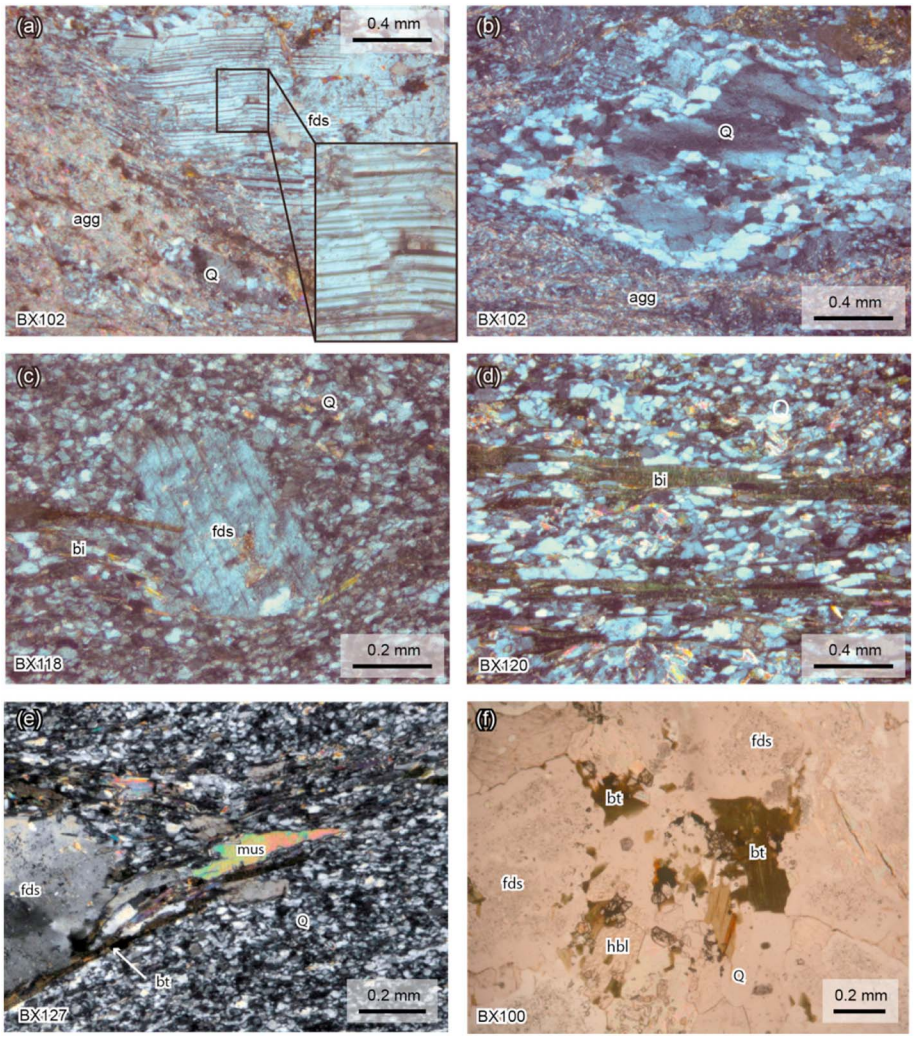

Figure 5. Microscopic features of dated samples. (a) Brittle kink bands and tapering deformation twins in feldspar, surrounded by quartz subgrains and mineral aggregates formed by fine-grained mica, quartz, and feldspar (sample BX102). (b) Undulose extinction in remnant quartz core, surrounded by elongated and recrystallized quartz subgrains in sample BX102. (c) Feldspar surrounded by elongated and recrystallized quartz subgrains (BX118). (d) Dynamically recrystallized quartz formed by subgrain rotation recrystallization (BX120). Biotite in this sample is elongated and aligned along the shear foliation. (e) Elongated white mica and biotite, distributed in the pressure shadow around a porphyroclast in sample BX127. The subhorizontally distributed mineral aggregate (Figures 5a and 5b), biotite (Figures 5c–5e), and white mica (Figure 5d) define the shear foliation. See Figure 3 and Table 1 for sample locations. (f) Microscope photo of undeformed sample BX100. Biotite in the sample is subhedral.

Biotite microprobe results show evident compositional differences between deformed and undeformed samples (Figure 9). Biotite from the undeformed sample BX100 has higher FeO (27–35 wt %) and TiO_2 (2.1–3.2 wt %) contents and lower MgO content (1–3 wt %) compared to mylonitized samples (BX118, BX120, and BX127), whose FeO, TiO_2, and MgO content is10–29 wt %, 0.9–2.0 wt %, and 5–17 wt %, respectively (Figures 9b and 9c). In the Al–Mg–Fe ternary plot, the undeformed biotite of BX100 falls on the boundary between the peraluminous (P) and alkaline (A) fields, whereas all deformed biotite fall into the calc-alkaline (C) field, or onto the calc-alkaline (C) and peraluminous (P) boundary (Figure 9d). These results indicate that biotite composition may have changed significantly during mylonitization by recrystallization, consistent with the petrographic observations that these biotite grains are elongated and aligned along the shear foliation (Figures 5c–5e). Furthermore, the K_2O content (7–10.3 wt %) in all biotite samples is lower than that of pure biotite (11%); this may be related to partial chloritization observed in all samples (Table 1).

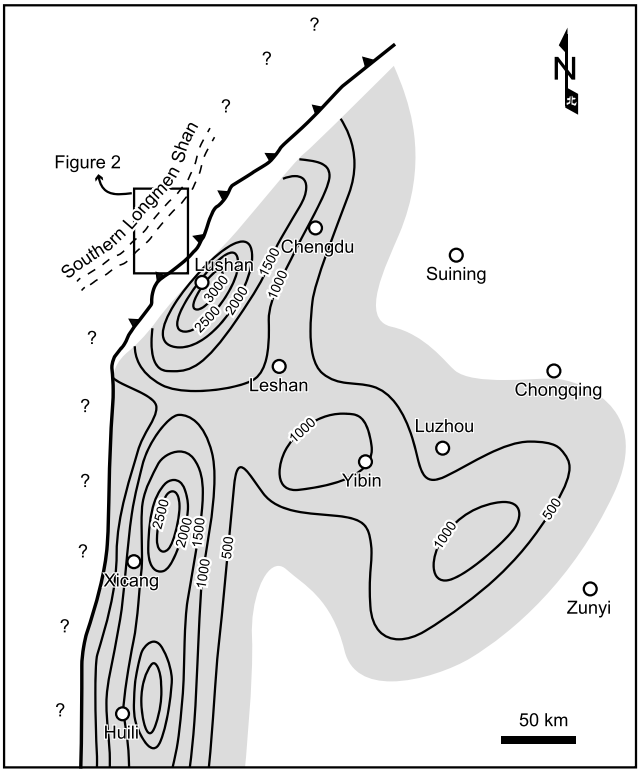

Figure 6. Isopach map (m) for Late Cretaceous–early Paleogene sedimentation in the southwestern Sichuan Basin, modified after *Guo et al.* [1996]. Development of the foredeep in front of the southern Longmen Shan required significant thrust loading along the southwestern margin of the Sichuan Basin. The approximate location of Figure 2 is marked for comparison.

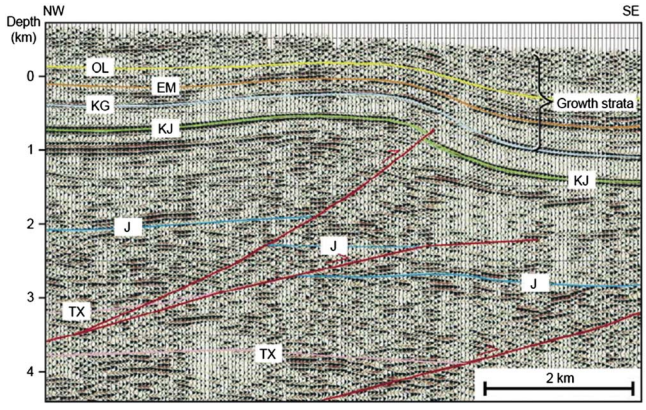

Figure 7. A seismic profile oriented across the Longmen Shan front, modified from *Jia et al.* [2006]. See Figure 2 for location. Note the Late Cretaceous–Paleogene growth strata in the forelimb of an anticline, indicating coeval crustal shortening at the Longmen Shan front, which is interpreted here as D_2^2. Abbreviations (from young to old): OL = base of Oligocene (Lushan Formation), EM = base of Eocene and Paleocene (Mingshan Formation), KG = base of uppermost Cretaceous (Guankou Formation), KJ = base of Lower Cretaceous (Jiaguan Formation), J = base Jurassic, and TX = base of Upper Triassic (Xujiahe Formation).

White mica from samples BX118 and BX127 have similar chemistry, except for Ti (Figure 10 and Table S1). These white mica occurrences show an evident deviation from the end-member muscovite. They are phengitic and Si^{4+} varies between 6.60 and 6.75, as calculated based on 22 oxygens (Figure 10a). The white mica compositions also deviate from the ideal muscovite-phengite tie line, and this may result from the increase of Fe and Mg replacing Al and to partial alteration (chloritization), as shown by the negative relationship between the Mg + Fe (atu) and Al (atu) (Figure 10b). The compositional deviation from muscovite is consistent with petrographic observations that they are elongated and form the mylonite foliation (Figure 5e). Therefore, similar to biotite in the mylonite, the phengitic white mica was formed by recrystallization during mylonitization.

5.2. $^{40}Ar/^{39}Ar$ Geochronological Results

In samples, except for sample BX102, the biotite and white mica separates yield reasonably concordant age spectra, although sufficient discordance exists in some samples (BX120 and BX127) to preclude the calculation of plateau ages. White mica and biotite from the mylonite samples (BX102, BX118, BX120, and BX127) yield plateau and/or weighted mean ages ranging between 58 and 75 Ma (Figures 11a–11f and Table 2). The biotite $^{40}Ar/^{39}Ar$ age (61.0 ± 0.2 (2σ, if not specified) Ma) from the mylonite sample BX127 is slightly older by ~2% than the white mica age (59.4 ± 0.5) from the same sample. The inverse isochron plot of the biotite data indicates an initial $^{40}Ar/^{36}Ar$ ratio of 304 ± 24 (Figure S1), close to the atmospheric ratio (295.5), suggesting the absence of excess ^{40}Ar in the biotite sample.

Staircase age spectra are observed for the mineral aggregate sample BX102 (Figure 11e), white mica samples

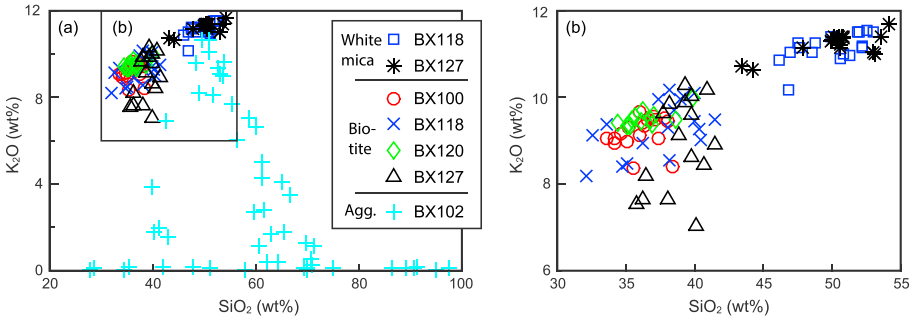

Figure 8. (a) SiO_2 versus K_2O plots for all samples. The plot shows that the mineral aggregate of sample BX102 has significant variations in SiO_2 and K_2O content. (b) A close-up view of SiO_2 versus K_2O plot of white mica and biotite samples. White mica has higher SiO_2 and K_2O content than biotite.

BX118 and BX127 (Figures 11a and 11c), and biotite sample BX120 (Figure 11f). This pattern is most evident for the fine-grained mineral aggregate, which exhibits ages increasing from ~40–30 Ma to ~69–65 Ma from low- to high-temperature steps (Figure 11e). Other age spectra include relatively young ages (75–40 Ma) from initial low-temperature steps, representing <20% of the total ^{39}Ar released but older and more consistent ages (73–59 Ma) for intermediate and high-temperature steps (Figures 8a, 8c, and 8f). Biotite age spectra of samples BX118 and BX127 are relatively flat, yielding plateau ages of 61–58 Ma (Figures 11b and 11d).

Compared to ages from the mylonite sample, biotite from the undeformed granite sample BX100 yields an older age, with the age spectrum characterized by an initial age increase from ~119 Ma to ~124 Ma followed by a decrease to ~115 Ma from low- to high-temperature steps (Figure 11g and Table 2). The low- to intermediate-temperature steps of the age spectrum yield an age plateau at 119.8 ± 1.6 Ma.

To summarize, the $^{40}Ar/^{39}Ar$ analyses show that (1) white mica and mineral aggregates have staircase age spectra, whereas the biotite age spectra are flat and (2) the mylonite samples have younger ages (~75–58 Ma) than the undeformed granite (~120 Ma).

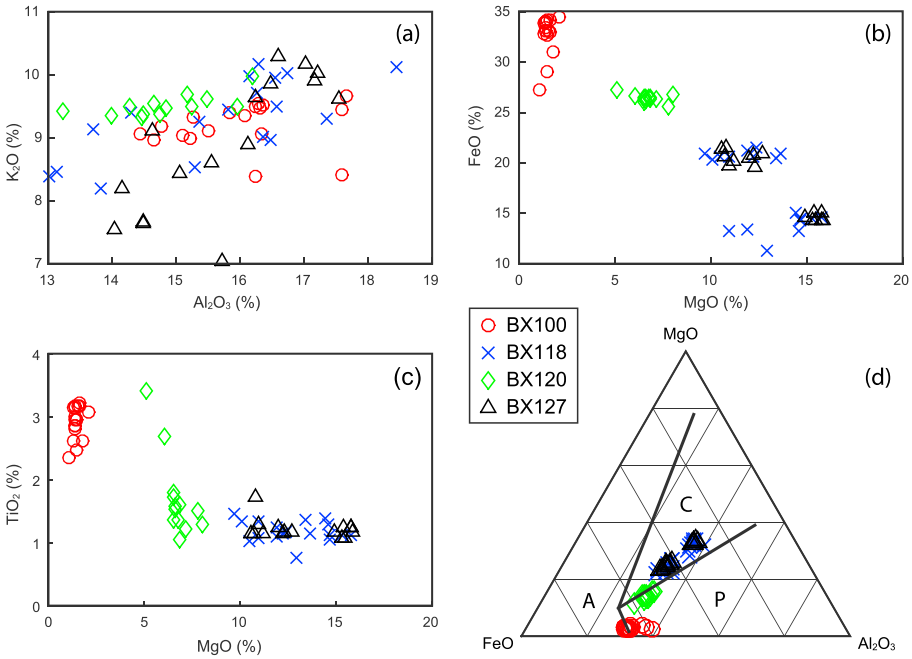

Figure 9. (a) Al_2O_3 versus K_2O, (b) MgO versus FeO (total Fe as FeO), and (c) MgO versus TiO_2 scatterplots for all biotite samples. (d) Ternary plot of Al_2O_3, MgO, and FeO content of all biotite samples. Fields for alkaline (A), calc-alkaline (C) field, and peraluminous (P) as defined by *Abdel-Rahman* [1994].

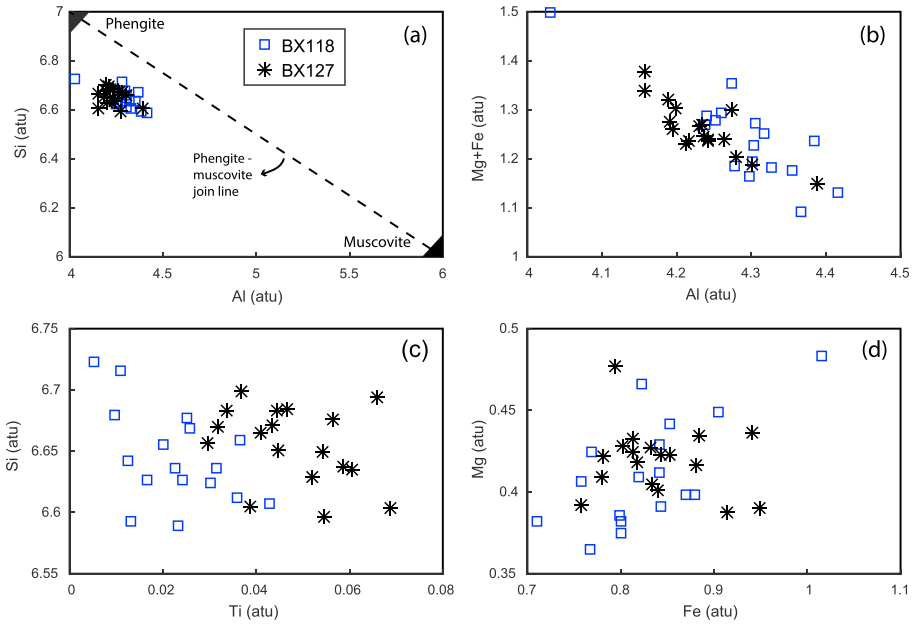

Figure 10. (a) Al (atu) versus Si (atu), (b) Al (atu) versus Mg + Fe (atu), (c) Ti (atu) versus Si (atu), and (d) Fe (atu) versus Mg (atu) plots for white mica samples. Most elements are similar in content in the two samples, except for Ti and Al.

5.3. $^{40}Ar/^{39}Ar$ Data Interpretation

The biotite age of sample BX100 is evidently older than white mica and biotite ages from other samples, even though they are geographically close to each other (within 1.5 km). This age is unlikely to have resulted from the presence of excess ^{40}Ar for the following reasons. (1) The age spectra of this sample are flat, whereas those with excess ^{40}Ar are often irregular [e.g., *McDougall and Harrison*, 1999]. (2) The inverse isochron plot of the sample indicates an initial $^{40}Ar/^{36}Ar$ ratio of 288 ± 30 (Figure S1), close to the atmospheric ratio (295.5), suggesting the absence of excess ^{40}Ar in the biotite sample. The $^{40}Ar/^{39}Ar$ age is significantly younger than the Precambrian rock crystallization age, indicating significant loss of radiogenic ^{40}Ar after emplacement. Considering that the dated biotite grains are undeformed (Figure 5f), the loss of ^{40}Ar is likely to have resulted from hydrothermal alteration or thermal diffusion. On the basis of these results, the Early Cretaceous age of the sample BX100 is interpreted as resulting from the partial resetting of Precambrian biotite $^{40}Ar/^{39}Ar$ system during the Late Cretaceous.

There are several possibilities that might account for the presence of younger ages in the initial steps of the white mica age spectra (Figures 11a and 11c). First, chemical alteration of white mica has been suggested as a possible mechanism to cause loss of ^{40}Ar and younger ages [e.g., *Hames and Cheney*, 1997; *Allaz et al*., 2011; *Verdel et al*., 2012]. Petrographic observations and EMPA results indicate partial alteration of the white mica and biotite. Interestingly, in our samples the form of the mylonite biotite age spectra does not appear to have been adversely influenced by the effects of alteration (Figures 11b, 11d and 11f), in contrast to studies from other areas [e.g., *Di Vincenzo et al*., 2003; *Allaz et al*., 2011]. Furthermore, it is also likely that the younger ages in the initial degassing steps were caused by thermally induced diffusive loss of ^{40}Ar during Cenozoic exhumation, given that similar to K-feldspars, muscovite may contain a distribution of ^{40}Ar diffusion domains [e.g., *McDougall and Harrison*, 1999; *Harrison et al*., 2009]. The above interpretations are supported by the presence of the Cenozoic deformation phase (see above) and Miocene zircon (U-Th)/He cooling ages that record significant late Cenozoic exhumation of the mylonite [*Tian et al*., 2013].

The staircase age spectrum of the mineral aggregate in sample BX102 (consisting of a mixture of micas, feldspar and quartz; Figure 8a) is commonly observed in fine-grained mineral mixes [e.g., *Kirschner et al*., 1996; *Fergusson and Phillips*, 2001]. The obviously younger middle–early Cenozoic ages (30–60 Ma) observed in the first degassing steps suggest partial loss of ^{40}Ar during the Cenozoic. This loss most likely results from the complex composition of the aggregate, as shown by both petrographic and EMPA results (Table 1 and Figure 8a).

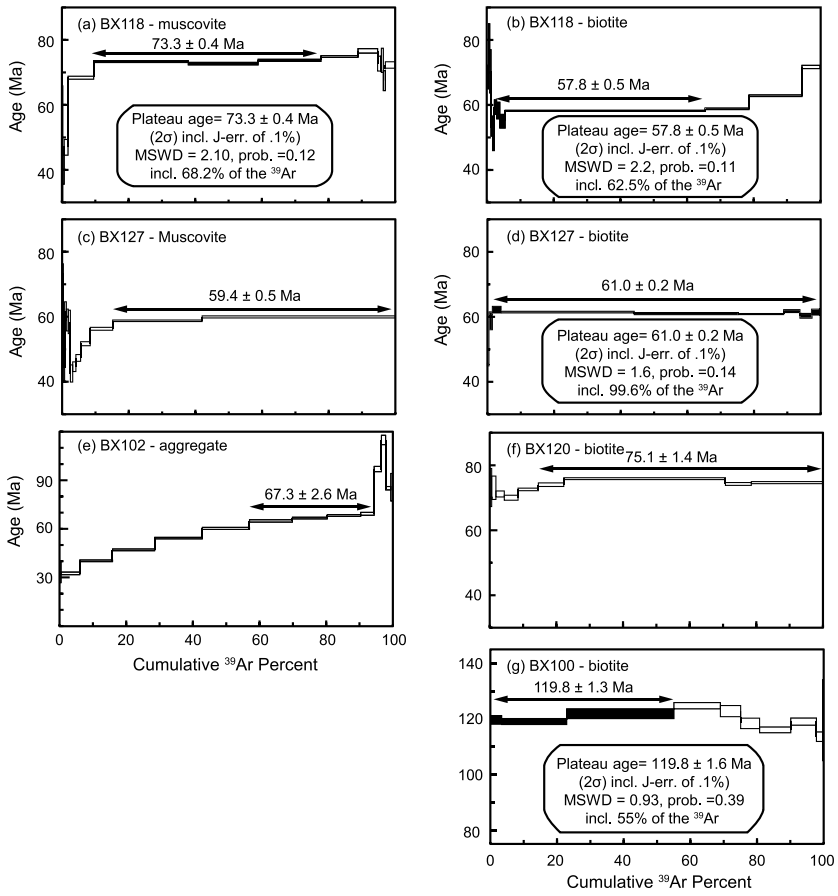

Figure 11. $^{40}Ar/^{39}Ar$ spectra plots. Steps filled in black are those fulfilling requirements for calculating plateau ages. Results and statistics related to plateau age calculations are summarized in the lower panel of relevant plots. Arrows above the age spectra show the range of steps used for calculating weighted mean ages (above the arrows). Age calculation results are summarized in Table 2, and detailed step-heating results are presented in the supporting information Text S2.

Other mechanisms, such as chemical alteration (see above) or diffusive loss during Cenozoic cooling, may also be possible. Furthermore, recoil loss and redistribution (between high- and low-potassium phases) of ^{39}Ar during irradiation of fined-grained minerals in a nuclear reactor may result in apparently older ages and negatively stepped age spectra [e.g., *McDougall and Harrison*, 1999; *Fergusson and Phillips*, 2001]. The total gas age of sample BX102 (58.6 ± 1.4 Ma) is slightly younger than those of other mylonite samples (75–58 Ma), consistent with predominant partial loss of ^{40}Ar, as discussed above, and more limited ^{39}Ar recoil effects.

Table 2. Summary of $^{40}Ar/^{39}Ar$ Dating Results

Sample No.	Mineral	[a]Plateau Age (Ma ± 2σ)	[a]Weighted Mean Age (Ma ± 2σ)	% ^{39}Ar in Plateau or Weighted Mean Age (Ma ± 2σ)	Total Gas Age (Ma ± 2σ)
BX100	Biotite	119.8 ± 0.8	119.8 ± 1.3	55%	120.5 ± 2.4
BX102	Aggregate	-	67.3 ± 2.6	38%	58.6 ± 1.4
BX118	Biotite	57.8 ± 0.5	57.8 ± 0.5	63%	59.2 ± 0.8
BX118	White mica	73.3 ± 0.4	73.3 ± 0.4	68%	72.7 ± 1.0
BX120	Biotite	-	75.1 ± 1.4	85%	73.9 ± 0.4
BX127	Biotite	61.0 ± 0.2	61.0 ± 0.2	100%	61.1 ± 0.6
BX127	White mica	-	59.4 ± 0.5	85%	58.8 ± 0.4

[a]Calculated using Isoplot [*Ludwig*, 1991].

Nonetheless, a process is required to explain the presence of the consistent Late Cretaceous–earliest Paleogene plateau or weighted mean ages (for the intermediate and high temperature steps) in all deformed samples. Dynamic recrystallization, intragrain deformation, and thermal resetting are two mechanisms for resetting Ar isotopic systematics [e.g., *Kirschner et al*., 1996; *McDougall and Harrison*, 1999; *Mulch and Cosca*, 2004; *Cosca et al*., 2011]. Biotite and white mica in the mylonite samples are strongly deformed and aligned along the shear foliation (Figures 4 and 5), suggesting that dynamic recrystallization during shearing probably reset the Ar isotopic systematics, as reported from other foliated rocks [e.g., *Kirschner et al*., 1996; *Dunlap*, 1997; *Mulch and Cosca*, 2004], and experimentally sheared samples [*Cosca et al*., 2011]. This interpretation is supported by the petrographic and EMPA results, showing significant differences in biotite texture and composition between deformed and undeformed samples. Recrystallization during mylonitization appears to have completely reset the Ar systematics. From this perspective, these Late Cretaceous–earliest Paleogene $^{40}Ar/^{39}Ar$ ages are interpreted as the time of recrystallization and thus mylonitization.

Alternatively, argon systematics can be reset at high temperatures, in which case the mineral $^{40}Ar/^{39}Ar$ ages could be interpreted as cooling ages [e.g., *McDougall and Harrison*, 1999]. In this scenario, we would expect that $^{40}Ar/^{39}Ar$ ages from the narrow mylonite zone (~2 km wide) to be comparable, considering that they were exhumed from a similar depth. However, this is inconsistent with the observation that the undeformed granite sample BX100 from the mylonite zone yields a significantly older biotite age (119.8 ± 1.6 Ma) than the nearby mylonite samples. Thus, we argue that thermal overprinting was not the main process for resetting the $^{40}Ar/^{39}Ar$ systematics of the current samples. Similar findings have been reported in low-grade mylonites from other deformation belts [e.g., *Dunlap*, 1997; *Mulch and Cosca*, 2004; *Kellett et al*., 2016].

6. Discussion

6.1. Lateral Comparison of Top-to-the-WNW Shear Deformation

Similar Late Cretaceous–earliest Paleogene top-to-the-WNW shear has been reported in the Danba Antiform, immediately south of the area (Figure 1b) [*Xu et al*., 2008; *Zhou et al*., 2008]. In that area, shearing was found to be associated with lower greenschist facies metamorphism, as indicated by a chlorite-biotite-muscovite-quartz mineral assemblage. $^{40}Ar/^{39}Ar$ biotite and muscovite ages from the deformation domain are 81–47 Ma [*Zhou et al*., 2008]. The characteristics of the top-to-the-WNW shear in the Danba Antiform are similar to those observed in the study area of this work. Considering the adjacent location of the two areas, it is likely that the Late Cretaceous–earliest Paleogene top-to-the-WNW shear may have extended ~200 km from the Longmen Shan to the Danba Antiform.

On the basis of a rapid phase of cooling between 65 and 50 Ma, *Wallis et al*. [2003] argued for an early Cenozoic phase of Barrovian metamorphism and N-S crustal shortening in the Danba Antiform. These geochronology results are similar to those reported from other studies [*Huang et al*., 2003; *Xu et al*., 2008; *Zhou et al*., 2008]. However, the structural results and interpretations are at odds with other detailed structural, petrological, and geochronological studies, which support Late Triassic–Early Jurassic Barrovian metamorphism and shortening [*Huang et al*., 2003; *Weller et al*., 2013], followed by a phase of top-to-the-WNW shearing, which is interpreted as resulting from Late Cretaceous–earliest Paleogene extension [*Xu et al*., 2008; *Zhou et al*., 2008].

In areas to the north of the study area, no evidence for Late Cretaceous–earliest Paleogene top-to-the-WNW shearing has been reported. Detailed structural studies by *Yan et al*. [2011] identified a phase of top-to-the-SE normal faulting in the northern Longmen Shan based on several lines of evidence: (i) juxtaposition of Silurian strata over the Precambrian basement, (ii) ductile deformation zones containing a 10–50 cm thick phyllonite and mylonite, showing top-to-the-SE normal faulting, and (iii) presence of a high angle normal fault between Jurassic sediments and older strata. *Yan et al*. [2011] also reported three early Jurassic $^{40}Ar/^{39}Ar$ muscovite ages (193–159 Ma) from the ductile normal faulting domain that may constrain the timing of this deformation. The early Jurassic normal faulting in the northern Longmen Shan differs in both the timing and sense of shear from the Late Cretaceous–earliest Paleogene deformation in the southern Longmen Shan and Danba Antiform. If the difference in sense of shear was caused by reorientation during the late Cenozoic shortening, a massive clockwise rotation by 90–120° would be required, predicting a significant rotation of the Sichuan Basin. However, such rotation is not observed from paleomagnetic studies [*Enkin et al*., 1991; *Huang and Opdyke*, 1992].

6.2. Late Cenozoic Tectonic Imprint

Within the WMF fault zone, where unambiguous top-to-the-WNW shear features are preserved, structural indicators showing SE verging reverse faulting are also observed. These structures are mostly brittle or brittle-ductile, and coplanar with top-to-the-WNW shear. These features are interpreted as resulting from the late Cenozoic crustal shortening, shown by late Cenozoic structures in the basin front and significant (~7–10 km) rock exhumation inferred from thermochronological data (see section 2 for details). Based on this interpretation, it is speculated that Paleozoic strata, exposed between the two sheets of Neoproterozoic basement rocks (Figure 2a), which show evidence of top-to-the-WNW shear (Figures 4e1 and e2), are allochthonous and were juxtaposed above the eastern sheet of the basement rocks during late Cenozoic SE verging thrusting (Figure 2e). This explanation differs from that given by *Burchfiel et al*. [1995] and *Cook et al*. [2013], which interpreted the shear in those Paleozoic strata as indicating a Cenozoic normal fault penetrating through the Paleozoic sequence down to basement rocks at depth.

6.3. Dynamics of Late Cretaceous–Earliest Paleogene Shear

Several geological and geophysical studies suggest that the Longmen Shan fold-and-thrust belt is thin skinned, characterized by a set of listric reverse faults that merge into a detachment at depths of ~20–30 km [*Tian et al*., 2013, and references therein]. Such a crustal geometry is considered to have been inherited from early Mesozoic intracontinental shortening between the Songpan-Ganze terrane and the Sichuan Basin [e.g., *SBGMR*, 1991; *Burchfiel et al*., 1995; *Chen et al*., 1995; *Tian et al*., 2013].

The Late Cretaceous–earliest Paleogene structural architecture, including contemporaneous top-to-the-hinterland shearing and top-to-the-foreland shortening in the hinterland and foreland sides, respectively, is also thin skinned. No high-pressure-temperature metamorphic minerals and no Late Cretaceous–earliest Paleogene magmatism have been reported in the study area. The deformation is therefore considered to have occurred under low-pressure-temperature conditions (greenschist metamorphic grade).

Previous studies interpreted the top-to-the-WNW shear as resulting from crustal extension [e.g., *Burchfiel et al*., 1995; *Xu et al*., 2008; *Zhou et al*., 2008]. In this case, a normal fault would be expected in areas west of the mylonite zone. The significantly attenuated Ordovician-Devonian cover rocks, which are mechanically weak shale and salt, may have hosted the normal fault. If the above interpretation is correct, the Late Cretaceous–earliest Paleogene crustal configuration would be characterized by extension in the hinterland and shortening in the foreland. Such a deformation pattern would indicate that the Late Cretaceous–earliest Paleogene Longmen Shan tectonics was controlled by crustal wedge extrusion (Figure 12a). This tectonic model has been used for explaining similar structural configurations in other regions [e.g., *Burchfiel et al*., 1992] and implies that under conditions of compression, extrusion of a hinterland-tapering crustal wedge forms an extruded crustal wedge, bounded by a thrust on the foreland side and a normal fault on the hinterland side. This interpretation would predict an extensional basin in the hanging wall side of the extensional zone. However, Late Cretaceous–earliest Paleogene sediments have not been mapped in the hinterland areas (Figure 2a). It is also possible that the extensional basin might have been removed by significant Cenozoic denudation [e.g., *Arne et al*., 1997; *Kirby et al*., 2002; *Tian et al*., 2013].

Alternatively, top-to-the-hinterland shearing could also be formed by crustal duplexing (Figure 12b). This model infers that a crustal wedge, bounded by a forelandward floor thrust and a hinterlandward roof thrust, is formed by numerous imbricate thrust faults branching off from a floor thrust and curve upward to join a roof thrust. The roof thrust can have an opposite sense-of-shear to the floor thrust [*Price*, 1986; *Webb et al*., 2007, 2011]. The top-to-the-hinterland shear observed in the hinterland areas of the Longmen Shan may correspond to the deformation along the roof thrust in the model. This model is consistent with the regional W-E contraction stress field and the development of the coeval foreland basin east of the Longmen Shan.

A third model, channel flow of middle and/or lower crust, can also produce a crustal configuration characterized by contemporaneous hinterlandward shear and forelandward shortening [e.g., *Beaumont et al*., 2001, and references therein]. The model involves melt-weakened middle and/or lower crust, driven by topographic loading in an orogen interior and surface erosion at the orogen front, that decouples from the upper crust and flows outward toward the orogen front. Decoupling between the flowing middle and/or lower crust and upper crust forms a ductile hinterlandward shear zone on the backside of the flow channel and a thrust fault on the frontal side (Figure 12c). One of the many features of this model is the presence of molten material

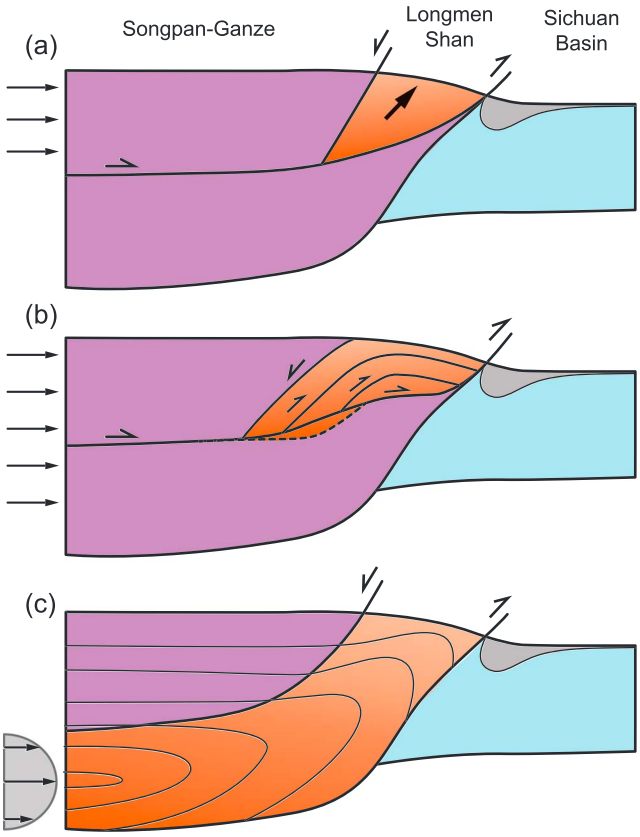

Figure 12. Possible models for explaining contemporaneous Late Cretaceous–earliest Paleogene top-to-the-hinterland shear and foreland thrusting in the Longmen Shan. (a) Crustal wedge extrusion model. Extrusion of a crustal wedge forms a crustal configuration with extensional zone and a shortening zone in the hinterland and foreland, respectively. (b) Duplex model. This model infers that a crustal wedge, bounded by a forelandward floor thrust and a hinterlandward roof thrust, is formed by numerous imbricate thrust faults branching off from a floor thrust, which curve upward to join a roof thrust. The roof thrust can have a top-to-the-hinterland sense of shear, opposite sense-of-shear to the floor thrust. (c) Lower crustal flow model. Outward extrusion of melt-weakened lower crust forms a normal fault and a thrust at the back and front of the flow channel, respectively (modified from *Beaumont et al.* [2001]).

(e.g., leucogranitic magmatism). However, such magmatism is absent from the Cretaceous–Cenozoic Longmen Shan. The youngest granitic intrusion in the Longmen Shan is late Jurassic, whereas younger plutons occur in areas along and south of the Xianshuihe fault [e.g., *Roger et al.*, 2008].

6.4. Inherited Topographic Relief and Crustal Thickness

Contemporaneous intracontinental hinterlandward shear and foreland shortening has been recognized in other orogenic belts, such as the Miocene Himalayas (introduced above), Late Devonian Quebec Appalachians [e.g., *Pinet et al.*, 1996; *Castonguay et al.*, 2007], Scandinavian Caledonides [e.g., *Hartz and Andresen*, 1997; *Grimmer et al.*, 2015], central East Greenland Caledonides [e.g., *White and Hodges*, 2002; *Johnston et al.*, 2010], and the Alpine orogen [e.g., *Tavarnelli*, 1999; *Schmid et al.*, 2004; *Selverstone*, 2005]. This kind of intracontinental deformation has been recognized during both synorogenic and postorogenic periods in these orogens. Although the detailed processes and mechanisms for forming the structural combination vary fundamentally from one case to another, a common feature is that it occurs in regions with thickened crust [e.g., *Hartz and Andresen*, 1997; *Yin and Harrison*, 2000; *Schmid et al.*, 2004; *Grimmer et al.*, 2015]. It is therefore reasonable to suggest that Longmen Shan crust had reached a considerable thickness by the Late Cretaceous–earliest Paleogene. This inference is consistent with the development of (1) a Late Triassic–early Jurassic thickened crust as indicated by the coeval Barrovian metamorphism and shortening [*Huang et al.*, 2003; *Weller et al.*, 2013] and (2) a Late Cretaceous–early Paleogene ~2–3 km foredeep in the southwestern Sichuan Basin (Figure 6), indicating a high topographic load above the western margin.

6.5. Implications for Regional Cenozoic Tectonics

If correct, the interpretation of a pre-Cenozoic thickened crust in the Longen Shan region would have important implications for the Cenozoic paleoaltimetry and tectonics of the eastern Tibetan Plateau. This interpretation is consistent with paleoaltimetric studies using oxygen isotopes by *Hoke et al.* [2014], which suggested that the southeastern Tibetan Plateau had reached its present high elevation by as early as late Eocene time. Further, it is likely that some of the present crustal thickness (~60 km) is inherited from the Mesozoic, highlighting the role of late Mesozoic tectonics in forming the thickened crust in the present eastern Tibetan Plateau, as proposed for other areas of the Tibetan Plateau [e.g., *England and Searle*, 1986; *Murphy et al.*, 1997; *Kapp et al.*, 2003; *Robinson et al.*, 2004].

Furthermore, possible pre-Cenozoic thickened crust has implications for geodynamic models proposed for explaining the Cenozoic deformation and the formation of the present thickened crust in the eastern Tibetan Plateau. The models can be categorized into two end-member models—the upper crustal shortening model [e.g., *Tapponnier et al*., 2001; *Hubbard and Shaw*, 2009; *Tian et al*., 2013] and the lower crustal flow model [e.g., *Burchfiel et al*., 1995, 2008; *Clark et al*., 2005; *Royden et al*., 2008]. The first model argues that shortening in the Longmen Shan was triggered by eastward movement of the upper crust of the Songpan-Ganze terrane along a detachment fault at a depth of ~20–30 km. The thrust rocks were backstopped, piled up, and thrust upward by steeply NW dipping, out-of-sequence reverse faults beneath the Longmen Shan, thus building up the thickened crust and high elevations in the eastern Tibetan Plateau [*Tian et al*., 2013]. The other end-member model, the lower crustal flow model, infers that the flow of ductile lower crustal material away from the central Tibetan Plateau, impeded by the strong crust of the Yangtze Craton beneath the Sichuan Basin, would increase topographic relief in the Longmen Shan by inflating its lower crust [e.g., *Burchfiel et al*., 1995, 2008; *Clark et al*., 2005; *Royden et al*., 2008]. In this model, the upper crust responds passively to the extrusion of deeper materials; thus, late Cenozoic normal faulting is predicted along the backside of the "channel," which is regarded as the WMF [e.g., *Burchfiel et al*., 2008; *Royden et al*., 2008].

As to the upper crustal shortening model, the pre-Cenozoic thickened crust explains the formation of the present eastern Tibetan Plateau margin under limited upper crustal convergence. Interseismic GPS observations indicate that upper crustal NW-SE shortening along the Longmen Shan is no more than 2–3 mm/yr [e.g., *Zhang et al*., 2004]. Further, on the foreland side, no apparent deep late Cenozoic flexural basins were developed, suggesting that total crustal shortening across the Longmen Shan was perhaps limited [*Burchfiel et al*., 1995]. Such restricted convergence would be difficult to reconcile with a scenario for the formation of the thickened crust of the Longmen Shan. However, since the Longmen Shan probably gained considerable crustal thickness in pre-Cenozoic time, significant convergence involving an upper crustal mechanism may not be required, even though it cannot be ruled out [*Tian et al*., 2013, and references therein].

Concerning the lower crustal flow model, as pointed out by *Rey et al*. [2010], a weak lower crust develops to allow lateral flow when a critical crustal thickness (~50 km) is reached, indicating that lower crustal flow is a consequence of crustal thickening, rather than its cause. If lower crustal flow did exist in the eastern Tibetan Plateau, it should be considered as a response to crustal thickening in both Cenozoic and pre-Cenozoic time, and its role in forming the thickened crustal should be minor and cannot be invoked to account for all the crustal thickening in this region of the plateau. Further, the timing of ductile hinterlandward shear in the Longmen Shan hinterland as reported here precludes it from being a response to late Cenozoic lower crustal flow, as proposed by previous studies [e.g., *Burchfiel et al*., 1995, 2008; *Clark et al*., 2005; *Royden et al*., 2008].

7. Conclusions

Structural, petrographic, mineral composition, and $^{40}Ar/^{39}Ar$ geochronological results reported in this work identify a phase of Late Cretaceous–earliest Paleogene (58–75 Ma) top-to-the-hinterland shearing on the hinterland (western) side of the Longmen Shan. This deformation is contemporaneous with SE verging thrusting on the foreland side. In the context of the regional geology, such a tectonic configuration could result either from extrusion of a crustal wedge or back thrust in a duplex.

The development of intensive intracontinental deformation and a deep foreland basin in the southwestern Sichuan Basin suggest that a thickened crust likely already existed in the Longmen Shan by Late Cretaceous–earliest Paleogene time. We therefore conclude that it is likely that the present overthickened crust in the eastern Tibetan Plateau is partly inherited from Mesozoic deformation events.

Acknowledgments

Y.T. is grateful to Z. Tian and Z. Yan for field assistance, to S. Szczepanski for assistance with the $^{40}Ar/^{39}Ar$ analyses, to C. Seiler for his expert advice on structural geology, and A. Beard of Birkbeck for his assistance in microprobe analyses. The University of Melbourne $^{40}Ar/^{39}Ar$ facility is supported by the National Collaborative Research Infrastructure Strategy AuScope program. This manuscript was improved substantially by constructive reviews of A. Webb, A. Robinson, D. Kellett, P. Kapp, and an anonymous reviewer and editorial work by N. Niemi. A more detailed discussion of the analytical methodology can be found in the supporting information [*Steiger and Jäger*, 1977; *Renne et al*., 1998; *McDougall and Harrison*, 1999]. The data for this paper are included in the manuscript and the associated supporting information.

References

Abdel-Rahman, A.-F. M. (1994), Nature of biotites from alkaline, calc-alkaline, and peraluminous magmas, *J. Petrol.*, *35*(2), 525–541, doi:10.1093/petrology/35.2.525.

Allaz, J., M. Engi, A. Berger, and I. M. Villa (2011), The effects of retrograde reactions and of diffusion on ^{40}Ar–^{39}Ar ages of micas, *J. Petrol.*, *52*(4), 691–716, doi:10.1093/petrology/egq100.

Arne, D., B. Worley, C. Wilson, S. F. Chen, D. Foster, Z. L. Luo, S. G. Liu, and P. Dirks (1997), Differential exhumation in response to episodic thrusting along the eastern margin of the Tibetan Plateau, *Tectonophysics*, *280*(3), 239–256.

Beaumont, C., R. A. Jamieson, M. H. Nguyen, and B. Lee (2001), Himalayan tectonics explained by extrusion of a low-viscosity crustal channel coupled to focused surface denudation, *Nature*, *414*(6865), 738–742.

Burchfiel, B. C., C. Zhiliang, K. V. Hodges, L. Yuping, L. H. Royden, D. Changrong, and X. Jiene (1992), The South Tibetan detachment system, Himalayan orogen: Extension contemporaneous with and parallel to shortening in a collisional mountain belt, *Geol. Soc. Am. Spec. Pap.*, *269*, 1–41, doi:10.1130/SPE269-p1.

Burchfiel, B. C., Z. Chen, Y. Liu, and L. H. Royden (1995), Tectonics of the Longmen Shan and adjacent regions, central China, *Int. Geol. Rev.*, *37*(8), 661–735.

Burchfiel, B. C., L. H. Royden, R. D. van der Hilst, B. H. Hager, Z. Chen, R. W. King, C. Li, J. Lü, H. Yao, and E. Kirby (2008), A geological and geophysical context for the Wenchuan earthquake of 12 May 2008, Sichuan, People's Republic of China, *GSA Today*, *18*(7), 4–11.

Castonguay, S., G. Ruffet, and A. Tremblay (2007), Dating polyphase deformation across low-grade metamorphic belts: An example based on $^{40}Ar/^{39}Ar$ muscovite age constraints from the southern Quebec Appalachians, Canada, *Geol. Soc. Am. Bull.*, *119*(7–8), 978–992, doi:10.1130/b26046.1.

Chang, E. Z. (2000), Geology and tectonics of the Songpan-Ganzi fold belt, southwestern China, *Int. Geol. Rev.*, *42*(9), 813–831.

Chen, S. F., C. J. L. Wilson, and B. A. Worley (1995), Tectonic transition from the Songpan-Garze fold belt to the Sichuan Basin, south-western China, *Basin Res.*, *7*(3), 235–253.

Clark, M. K., J. W. M. Bush, and L. H. Royden (2005), Dynamic topography produced by lower crustal flow against rheological strength heterogeneities bordering the Tibetan Plateau, *Geophy. J. Int.*, *162*(2), 575–590, doi:10.1111/j.1365-246X.2005.02580.x.

Cook, K. L., L. H. Royden, B. C. Burchfiel, Y.-H. Lee, and X. Tan (2013), Constraints on Cenozoic tectonics in the southwestern Longmen Shan from low-temperature thermochronology, *Lithosphere*, *5*(4), 393–406, doi:10.1130/l263.1.

Cosca, M., H. Stunitz, A.-L. Bourgeix, and J. P. Lee (2011), $^{40}Ar^*$ loss in experimentally deformed muscovite and biotite with implications for $^{40}Ar/^{39}Ar$ geochronology of naturally deformed rocks, *Geochim. Cosmochim. Acta*, *75*(24), 7759–7778, doi:10.1016/j.gca.2011.10.012.

Densmore, A. L., M. A. Ellis, Y. Li, R. J. Zhou, G. S. Hancock, and N. Richardson (2007), Active tectonics of the Beichuan and Pengguan faults at the eastern margin of the Tibetan Plateau, *Tectonics*, *26*, TC4005, doi:10.1029/2006TC001987.

Di Vincenzo, G., C. Viti, and S. Rocchi (2003), The effect of chlorite interlayering on $^{40}Ar?^{39}Ar$ biotite dating: An $^{40}Ar?^{39}Ar$ laser-probe and TEM investigations of variably chloritised biotites, *Contrib. Mineral. Petrol.*, *145*(6), 643–658, doi:10.1007/s00410-003-0472-z.

Ding, L., et al. (2013), Provenance analysis of the Mesozoic Hoh-Xil-Songpan-Ganzi turbidites in northern Tibet: Implications for the tectonic evolution of the eastern Paleo-Tethys Ocean, *Tectonics*, *32*, 34–48, doi:10.1002/tect.20013.

Dunlap, W. (1997), Neocrystallization or cooling? $^{40}Ar/^{39}Ar$ ages of white micas from low-grade mylonites, *Chem. Geol.*, *143*(3–4), 181–203.

England, P., and G. Houseman (1986), Finite strain calculations of continental deformation 2. Comparison with the India-Asia collision zone, *J. Geophys. Res.*, *91*, 3664–3676, doi:10.1029/JB091iB03p03664.

England, P., and M. Searle (1986), The Cretaceous-tertiary deformation of the Lhasa Block and its implications for crustal thickening in Tibet, *Tectonics*, *5*, 1–14, doi:10.1029/TC005i001p00001.

Enkin, R. J., Y. Chen, V. Courtillot, J. Besse, L. Xing, Z. Zhang, Z. Zhuang, and J. Zhang (1991), A Cretaceous pole from south China, and the Mesozoic hairpin turn of the Eurasian apparent polar wander path, *J. Geophys. Res.*, *96*, 4007–4027, doi:10.1029/90JB01904.

Fergusson, C. L., and D. Phillips (2001), $^{40}Ar/^{39}Ar$ and K–Ar age constraints on the timing of regional deformation, south coast of New South Wales, Lachlan Fold Belt: Problems and implications, *Aust. J. Earth Sci.*, *48*(3), 395–408, doi:10.1046/j.1440-0952.2001.00866.x.

Godard, V., R. Pik, J. Lavé, R. Cattin, B. Tibari, J. de Sigoyer, M. Pubellier, and J. Zhu (2009), Late Cenozoic evolution of the central Longmen Shan, eastern Tibet: Insight from (U-Th)/He thermochronometry, *Tectonics*, *28*, TC5009, doi:10.1029/2008TC002407.

Grimmer, J. C., J. Glodny, K. Druppel, R. O. Greiling, and A. Kontny (2015), Early- to mid-Silurian extrusion wedge tectonics in the central Scandinavian Caledonides, *Geology*, *43*(4), 347–350, doi:10.1130/g36433.1.

Guenthner, W. R., P. W. Reiners, and Y. Tian (2014), Interpreting date–eU correlations in zircon (U-Th)/He datasets: A case study from the Longmen Shan, China, *Earth Planet. Sci. Lett.*, *403*, 328–339, doi:10.1016/j.epsl.2014.06.050.

Guo, Z., K. Deng, and Y. Han (1996), *Formation and Evolution of the Sichuan Basin*, Geol. Publ. House, Beijing.

Hames, W. E., and J. Cheney (1997), On the loss of $^{40}Ar^*$ from muscovite during polymetamorphism, *Geochim. Cosmochim. Acta*, *61*(18), 3863–3872.

Harrison, T. M., P. Copeland, W. S. F. Kidd, and A. Yin (1992), Raising Tibet, *Science*, *255*(5052), 1663–1670, doi:10.1126/science.255.5052.1663.

Harrison, T. M., J. Célérier, A. B. Aikman, J. Hermann, and M. T. Heizler (2009), Diffusion of ^{40}Ar in muscovite, *Geochim. Cosmochim. Acta*, *73*(4), 1039–1051, doi:10.1016/j.gca.2008.09.038.

Hartz, E. H., and A. Andresen (1997), From collision to collapse: Complex strain permutations in the hinterland of the Scandinavian Caledonides, *J. Geophys. Res.*, *102*, 24,697–24,711, doi:10.1029/97JB02275.

Hoke, G. D., J. Liu-Zeng, M. T. Hren, G. K. Wissink, and C. N. Garzione (2014), Stable isotopes reveal high southeast Tibetan Plateau margin since the Paleogene, *Earth Planet. Sci. Lett.*, *394*, 270–278, doi:10.1016/j.epsl.2014.03.007.

Hu, S. B., L. J. He, and J. Y. Wang (2000), Heat flow in the continental area of China: A new data set, *Earth Planet. Sci. Lett.*, *179*(2), 407–419.

Huang, K., and N. D. Opdyke (1992), Paleomagnetism of Cretaceous to lower Tertiary rocks from southwestern Sichuan: A revisit, *Earth Planet. Sci. Lett.*, *112*(1–4), 29–40, doi:10.1016/0012-821X(92)90004-F.

Huang, M. H., I. S. Buick, and L. W. Hou (2003), Tectonometamorphic evolution of the Eastern Tibet Plateau: Evidence from the central Songpan–Garzê orogenic belt, Western China, *J. Petrol.*, *44*(2), 255–278, doi:10.1093/petrology/44.2.255.

Hubbard, J., and J. H. Shaw (2009), Uplift of the Longmen Shan and Tibetan plateau, and the 2008 Wenchuan ($M = 7.9$) earthquake, *Nature*, *458*(7235), 194–197.

Ji, S., A. Snoke, J. Tullis, and V. Todd (1998), Kink bands and recrystallization in plagioclase, in *Fault Related Rocks—A Photographic Atlas*, edited by A. W. Snoke, J. Tullis, and V. R. Todd, pp. 278–279, Princeton Univ. Press, Princeton, N. J.

Jia, D., G. Q. Wei, Z. X. Chen, B. L. Li, Q. Zen, and G. Yang (2006), Longmen Shan fold-thrust belt and its relation to the western Sichuan Basin in central China: New insights fiom hydrocarbon exploration, *AAPG Bull.*, *90*(9), 1425–1447.

Johnston, S. M., E. H. Hartz, H. K. Brueckner, and G. E. Gehrels (2010), U–Pb zircon geochronology and tectonostratigraphy of southern Liverpool Land, East Greenland: Implications for deformation in the overriding plates of continental collisions, *Earth Planet. Sci. Lett.*, *297*(3–4), 512–524, doi:10.1016/j.epsl.2010.07.003.

Kapp, P., M. A. Murphy, A. Yin, T. M. Harrison, L. Ding, and J. Guo (2003), Mesozoic and Cenozoic tectonic evolution of the Shiquanhe area of western Tibet, *Tectonics*, *22*(4), 1029, doi:10.1029/2001TC001332.

Kapp, P., P. G. DeCelles, G. E. Gehrels, M. Heizler, and L. Ding (2007), Geological records of the Lhasa-Qiangtang and Indo-Asian collisions in the Nima area of central Tibet, *Geol. Soc. Am. Bull.*, *119*(7–8), 917–933, doi:10.1130/b26033.1.

Kellett, D. A., C. Warren, K. P. Larson, H. Zwingmann, C. R. van Staal, and N. Rogers (2016), Influence of deformation and fluids on Ar retention in white mica: Dating the Dover Fault, Newfoundland Appalachians, *Lithos*, 254–255, 1–17, doi:10.1016/j.lithos.2016.03.003.

Kirby, E., P. W. Reiners, M. A. Krol, K. X. Whipple, K. V. Hodges, K. A. Farley, W. Q. Tang, and Z. L. Chen (2002), Late Cenozoic evolution of the eastern margin of the Tibetan Plateau: Inferences from $^{40}Ar/^{39}Ar$ and (U-Th)/He thermochronology, *Tectonics*, *21*(1), 1001, doi:10.1029/2000TC001246.

Kirschner, D. L., M. A. Cosca, H. Masson, and J. C. Hunziker (1996), Staircase $^{40}/Ar^{39}Ar$ spectra of fine-grained white mica: Timing and duration of deformation and empirical constraints on argon diffusion, *Geology*, *24*(8), 747–750, doi:10.1130/0091-7613(1996)024<0747:saasof>2.3.co;2.

Li, Y., P. A. Allen, A. L. Densmore, and X. Qiang (2003), Evolution of the Longmen Shan Foreland Basin (Western Sichuan, China) during the Late Triassic Indosinian orogeny, *Basin Res.*, *15*(1), 117–138.

Ludwig, K. R. (1991), ISOPLOT: A plotting and regression program for radiogenic-isotope data; version 2.53Rep., Open File Report 91-445, U. S. Geological Survey.

McDougall, I., and T. M. Harrison (1999), *Geochronology and Thermochronology by the $^{40}Ar/^{39}Ar$ Method*, Oxford Univ. Press, New York.

Meng, Q.-R., J.-M. Hu, E. Wang, and H.-J. Qu (2006), Late Cenozoic denudation by large-magnitude landslides in the eastern edge of Tibetan Plateau, *Earth Planet. Sci. Lett.*, *243*(1–2), 252–267.

Molnar, P. (1988), Continental tectonics in the aftermath of plate tectonics, *Nature*, *335*, 131–137.

Mulch, A., and M. A. Cosca (2004), Recrystallization or cooling ages: In situ UV-laser $^{40}Ar/^{39}Ar$ geochronology of muscovite in mylonitic rocks, *J. Geol. Soc.*, *161*(4), 573–582.

Murphy, M. A., A. Yin, T. M. Harrison, S. B. Durr, C. Z.,. F. J. Ryerson, W. S. F. Kidd, X. Wang, and X. Zhou (1997), Did the Indo-Asian collision alone create the Tibetan plateau?, *Geology*, *25*(8), 719–722, doi:10.1130/0091-7613(1997)025<0719:dtiaca>2.3.co;2.

Passchier, C. W., and R. A. J. Trouw (2005), *Microtectonics*, Springer Verlag, Heidelberg, Berlin.

Pinet, N., A. Tremblay, and M. Sosson (1996), Extension versus shortening models for hinterland-directed motions in the southern Québec Appalachians, *Tectonophysics*, *267*(1–4), 239–256, doi:10.1016/S0040-1951(96)00096-0.

Pollack, H. N., S. J. Hurter, and J. R. Johnson (1993), Heat flow from the Earth's interior: Analysis of the global data set, *Rev. Geophys.*, *31*, 267–280, doi:10.1029/93RG01249.

Price, R. A. (1986), The southeastern Canadian Cordillera: Thrust faulting, tectonic wedging, and delamination of the lithosphere, *J. Struct. Geol.*, *8*(3–4), 239–254, doi:10.1016/0191-8141(86)90046-5.

Renne, P. R., C. C. Swisher, A. L. Deino, D. B. Karner, T. L. Owens, and D. J. DePaolo (1998), Intercalibration of standards, absolute ages and uncertainties in $^{40}Ar/^{39}Ar$ dating, *Chem. Geol.*, *145*(1–2), 117–152, doi:10.1016/S0009-2541(97)00159-9.

Rey, P. F., C. Teyssier, and D. L. Whitney (2010), Limit of channel flow in orogenic plateaux, *Lithosphere*, *2*(5), 328–332, doi:10.1130/l114.1.

Richardson, N. J., A. L. Densmore, D. Seward, A. Fowler, M. Wipf, M. A. Ellis, L. Yong, and Y. Zhang (2008), Extraordinary denudation in the Sichuan Basin: Insights from low-temperature thermochronology adjacent to the eastern margin of the Tibetan Plateau, *J. Geophys. Res.*, *113*, B04409, doi:10.1029/2006JB004739.

Robinson, A. C., A. Yin, C. E. Manning, T. M. Harrison, S. H. Zhang, and X. F. Wang (2004), Tectonic evolution of the northeastern Pamir: Constraints from the northern portion of the Cenozoic Kongur Shan extensional system, western China, *Geol. Soc. Am. Bull.*, *116*(7–8), 953–973, doi:10.1130/b25375.1.

Roger, F., S. Calassou, J. Lancelot, J. Malavieille, M. Mattauer, X. Zhiqin, H. Ziwen, and H. Liwei (1995), Miocene emplacement and deformation of the Konga Shan granite (Xianshui He fault zone, west Sichuan, China): Geodynamic implications, *Earth Planet. Sci. Lett.*, *130*(1–4), 201–216, doi:10.1016/0012-821x(94)00252-t.

Roger, F., M. Jolivet, and J. Malavieille (2008), Tectonic evolution of the Triassic fold belts of Tibet, *C. R. Geosci.*, *340*(2–3), 180–189.

Royden, L. H., B. C. Burchfiel, and R. D. van der Hilst (2008), The geological evolution of the Tibetan Plateau, *Science*, *321*(5892), 1054–1058, doi:10.1126/science.1155371.

SBGMR (Sichuan Bureau of Geology and Mineral Resources) (1976), Geological map of the Baoxing area, scale 1:200,000, sheet G-48-XIII, Chengdu.

SBGMR (Sichuan Bureau of Geology and Mineral Resources) (1991), *Regional Geology of Sichuan Province*, pp. 728 , Geol. Publ. House, Beijing.

Schmid, S., B. Fügenschuh, E. Kissling, and R. Schuster (2004), Tectonic map and overall architecture of the Alpine orogen, *Eclogae Geol. Helv.*, *97*(1), 93–117, doi:10.1007/s00015-004-1113-x.

Selverstone, J. (2005), Are the alps collapsing?, *Annu. Rev. Earth Planet. Sci.*, *33*(1), 113–132, doi:10.1146/annurev.earth.33.092203.122535.

Steiger, R. H., and E. Jäger (1977), Subcommission on geochronology: Convention on the use of decay constants in geo- and cosmochronology, *Earth Planet. Sci. Lett.*, *36*(3), 359–362, doi:10.1016/0012-821X(77)90060.

Stipp, M., H. Stünitz, R. Heilbronner, and S. M. Schmid (2002), The eastern Tonale fault zone: A "natural laboratory" for crystal plastic deformation of quartz over a temperature range from 250 to 700°C, *J. Struct. Geol.*, *24*(12), 1861–1884.

Tao, X. (1999), Evolution of nappe tectonic and foreland basin in the southern section of Longmen mountains, *J. Chengdu Inst. Tech.*, *26*(2), 73–77.

Tapponnier, P., Z. Xu, F. Roger, B. Meyer, N. Arnaud, G. Wittlinger, and J. Yang (2001), Oblique stepwise rise and growth of the Tibet Plateau, *Science*, *294*(5547), 1671–1677, doi:10.1126/science.105978.

Tavarnelli, E. (1999), Normal faults in thrust sheets: Pre-orogenic extension, post-orogenic extension, or both?, *J. Struct. Geol.*, *21*(8–9), 1011–1018, doi:10.1016/S0191-8141(99)00034-6.

Tian, Y., B. P. Kohn, C. Zhu, M. Xu, S. Hu, and A. J. W. Gleadow (2012a), Post-orogenic evolution of the Mesozoic Micang Shan Foreland Basin system, central China, *Basin Res.*, *24*(1), 70–90, doi:10.1111/j.1365-2117.2011.00516.x.

Tian, Y., N. Qiu, B. P. Kohn, C. Zhu, S. Hu, A. J. W. Gleadow, and B. I. A. McInnes (2012b), Detrital zircon (U–Th)/He thermochronometry of the Mesozoic Daba Shan Foreland Basin, central China: Evidence for timing of post-orogenic denudation, *Tectonophysics*, *570–571*, 65–77, doi:10.1016/j.tecto.2012.08.010.

Tian, Y., B. P. Kohn, A. J. W. Gleadow, and S. Hu (2013), Constructing the Longmen Shan eastern Tibetan Plateau margin: Insights from low-temperature thermochronology, *Tectonics*, *32*, 576–592, doi:10.1002/tect.20043.

Verdel, C., B. A. van der Pluijm, and N. Niemi (2012), Variation of illite/muscovite $^{40}Ar/^{39}Ar$ age spectra during progressive low-grade metamorphism: An example from the US Cordillera, *Contrib. Mineral. Petrol.*, *164*(3), 521–536, doi:10.1007/s00410-012-0751-7.

Wallis, S., T. Tsujimori, M. Aoya, T. Kawakami, K. Terada, K. Suzuki, H. Hyodo, J. Qin, Z. Xia, and J. Tian (2003), Cenozoic and Mesozoic metamorphism in the Longmenshan orogen: Implications for geodynamic models of eastern Tibet, *Geology*, *31*(9), 745–748, doi:10.1130/g19562.1.

Wang, E., E. Kirby, K. P. Furlong, M. van Soest, G. Xu, X. Shi, P. J. J. Kamp, and K. V. Hodges (2012), Two-phase growth of high topography in eastern Tibet during the Cenozoic, *Nat. Geosci.*, *5*(9), 640–645, doi:10.1038/ngeo1538.

Wang, E., K. Meng, Z. Su, Q. Meng, J. J. Chu, Z. Chen, G. Wang, X. Shi, and X. Liang (2014), Block rotation: Tectonic response of the Sichuan basin to the southeastward growth of the Tibetan Plateau along the Xianshuihe-Xiaojiang fault, *Tectonics*, *33*, 686–718, doi:10.1002/2013TC003337.

Webb, A. A. G., A. Yin, T. M. Harrison, J. Célérier, and W. P. Burgess (2007), The leading edge of the Greater Himalayan Crystalline complex revealed in the NW Indian Himalaya: Implications for the evolution of the Himalayan orogen, *Geology*, *35*(10), 955–958, doi:10.1130/g23931a.1.

Webb, A. A. G., A. K. Schmitt, D. He, and E. L. Weigand (2011), Structural and geochronological evidence for the leading edge of the Greater Himalayan Crystalline complex in the central Nepal Himalaya, *Earth Planet. Sci. Lett.*, *304*(3–4), 483–495, doi:10.1016/j.epsl.2011.02.024.

Weller, O. M., M. R. St-Onge, D. J. Waters, N. Rayner, M. P. Searle, S. L. Chung, R. M. Palin, Y. H. Lee, and X. Xu (2013), Quantifying Barrovian metamorphism in the Danba Structural Culmination of eastern Tibet, *J. Metamorph. Geol.*, *31*(9), 909–935, doi:10.1111/jmg.12050.

White, A. P., and K. V. Hodges (2002), Multistage extensional evolution of the central East Greenland Caledonides, *Tectonics*, *21*(5), 1048, doi:10.1029/2001TC001308.

Xu, M., C. Zhu, Y. Tian, S. Rao, and S. Hu (2011), Borehole temperature logging and characteristics of subsurface temperature in Sichuan Basin, *Chin. J. Geophys.*, *54*(4), 1052–1060.

Xu, Z. Q., S. C. Ji, H. B. Li, L. W. Hou, X. F. Fu, and Z. H. Cai (2008), Uplift of the Longmen Shan range and the Wenchuan earthquake, *Episodes*, *31*(3), 291–301.

Yan, D.-P., M.-F. Zhou, S.-B. Li, and G.-Q. Wei (2011), Structural and geochronological constraints on the Mesozoic-Cenozoic tectonic evolution of the Longmen Shan thrust belt, eastern Tibetan Plateau, *Tectonics*, *30*, TC6005, doi:10.1029/2011TC002867.

Yin, A., and T. M. Harrison (2000), Geologic evolution of the Himalayan-Tibetan orogen, *Annu. Rev. Earth Planet. Sci.*, *28*(1), 211–280, doi:10.1146/annurev.earth.28.1.211.

Zhang, P., et al. (2004), Continuous deformation of the Tibetan Plateau from Global Positioning System data, *Geology*, *32*(9), 809–812, doi:10.1130/g20554.1.

Zhang, P.-Z., X.-Z. Wen, Z.-K. Shen, and J.-h. Chen (2010), Oblique, high-angle, listric-reverse faulting and associated development of strain: The Wenchuan earthquake of May 12, 2008, Sichuan, China, *Annu. Rev. Earth Planet. Sci.*, *38*(1), 353–382, doi:10.1146/annurev-earth-040809-152602.

Zhou, M.-F., D.-P. Yan, P. M. Vasconcelos, J.-W. Li, and R.-Z. Hu (2008), Structural and geochronological constraints on the tectono-thermal evolution of the Danba domal terrane, eastern margin of the Tibetan plateau, *J. Asian Earth Sci.*, *33*(5–6), 414–427, doi:10.1016/j.jseaes.2008.03.003.

Zhuang, Z. H., D. X. Tian, X. H. Ma, X. F. Ren, X. C. Jiang, and S. L. Xu (1988), A paleomagnetic study along the Ya'an-Tianquan Cretaceous–Eogene section in Sichuan Basin, *Geophys. Geochem. Explor.*, *12*, 224–228.